CHAPTER FIVE

Thermoelectric generators: A case study in multi-scale thermal engineering design

Marc T. Dunham[1,*], Terry J. Hendricks[2] and Kenneth E. Goodson[3]
[1]Analog Devices, Inc., San Jose, CA, United States
[2]Power and Sensors System Section, NASA-Jet Propulsion Laboratory, California Institute of Technology, Pasadena, CA, United States
[3]Department of Mechanical Engineering, Stanford University, Stanford, CA, United States
*Corresponding author: E-mail: mdunham@alumni.stanford.edu

Contents

Advances in Heat Transfer, Volume 51
ISSN 0065-2717
https://doi.org/10.1016/bs.aiht.2019.08.001

Abstract

In this chapter we review the fundamental principles of thermoelectric phenomena, devices, and optimization techniques, with a focus on the multi-scale design of thermoelectric energy generators (TEGs). TEG technology represents a fascinating case study of the interplay between thermal and electrical transport, with pronounced multi-scale impacts from nanoscale phonon and electron transport to the design of efficient heat exchangers in the optimization of a complete system. We explore several of these areas in detail, with particular attention given to the effects of temperature-dependent thermoelectric material properties on the optimal ratio of hot-to-cold side heat exchanger thermal resistances and the relation to the second law of thermodynamics in the macroscale system design. These conclusions are then connected to theory behind the design of thermoelectric materials through nanoengineering. Finally, we explore cost considerations related to TEG system heat exchanger design, offering a new perspective in the approach to the technoeconomic optimization of TEG power systems.

Nomenclature

English

A_{HEX}	TE/heat exchanger interface area [m^2]
A_{TE}	Thermoelectric element area [m^2]
C_{TEG}	Thermoelectric generator cost [$]
C_{HEX}	Heat exchanger cost parameter [$ ($W K^{-1}$) $^{-1}$]
C''	TE system manufacturing/fabrication costs per area [$ m^{-2}]
C'''	TE material volumetric costs per volume [$ m^{-3}]
C_p	Exhaust flow specific heat [J kg^{-1} K^{-1}]
F	Fill factor [−]
F_{opt}	Optimum cost fill factor [−]
G	Thermoelectric system cost per watt [$ W^{-1}]
I	Current [A]
K_{exh}	Heat exchanger conductance [W K^{-1}]
K_H	Hot side total thermal conductance [W K^{-1}]
K_C	Cold side total thermal conductance [W K^{-1}]
K_{HX}	Heat exchanger conductance value [W K^{-1}]
K_{TE}	Effective thermoelectric conductance [W K^{-1}]
l	Thermoelectric element length [m]
m	Load resistance ratio [−]
$\dot{m}_h$	Exhaust mass flow rate [kg sec^{-1}]
n_{TC}	Number of thermocouples [−]
P	Power [W]
q''	Heat flux [W m^{-2}]
$\dot{Q}$	Heat transfer rate [W]
R_e	Electrical resistance [Ω]
$R_{t,ext}$	Total external thermal resistance [K W^{-1}]
$R_{t,ext,h}$	Hot side thermal resistance [K W^{-1}]
$R_{th,ext,c}$	Cold side thermal resistance [K W^{-1}]
S	Seebeck coefficient [V K^{-1}]
T	Temperature [K]
UA_u	Heat exchanger *UA* value [W K^{-1}]

V	Voltage [V]
$\dot{X}$	Lost exergy [W]
Z	Thermoelectric material figure of merit [K^{-1}]
ZT	Dimensionless thermoelectric figure of merit = Z^*T

Greek

ΔT	Temperature Differential [K]
ε	Heat Exchanger Thermal Effectiveness
γ	Thermoelectric Element Length to Area Ratio [m^{-1}]
κ	Thermal Conductivity (thermoelectric material unless otherwise specified) [W m^{-1} K^{-1}]
η	Thermoelectric Conversion Efficiency
χ	Heat Loss Factor Quantifying Heat Losses (=Q_{loss} $Q_{h,TE}^{-1}$)

Subscripts

amb	ambient environment
exh	exhaust conditions
h	associated with hot-side parameter
c	associated with cold-side parameter
n	associated with TE n-type materials
p	associated with TE p-type materials
TE	Thermoelectric parameter
HEX	Heat Exchanger parameter

1. Introduction

Thermoelectric phenomena in materials result in the coupling of electric charge and thermal energy transport primarily through the Seebeck, Peltier, and Thomson effects. When properly assembled into a device architecture, materials exhibiting these effects enable the direct conversion of thermal energy to electricity in one configuration, or a heat pump developing a thermal gradient in response to an input of electric power. Thermoelectric effects are present to some degree in all materials with free electrons or holes, though they are most prominent and useful in a small subset of metals and semiconductors which present a favorable combination of thermal and electrical transport properties through the thermal and electrical conductivity parameters, as well as the thermally-driven electrical charge carrier diffusion captured by the Seebeck coefficient.

Metals with sufficient Seebeck coefficient are widely used for temperature measurement in thermocouples, as the temperature difference along the length of the metal wire is proportional to a developed electrical potential measured as a voltage. Various combinations of materials have become standardized as specific thermocouple types, for example the K-type thermocouples comprised of wires of nickel-chromium and nickel-alumel which

are welded together at one end to form a junction at which to probe temperature.

Semiconductors are more common in complex functional devices for thermal management and power generation applications, and most successful applications of thermoelectric devices rely on relatively complex materials. The most common set of basis materials for thermoelectric applications near room temperature utilizes thermocouples of bismuth telluride (Bi_2Te_3) and antimony telluride (Sb_2Te_3) compounds. Thermoelectric material properties are generally highly temperature-dependent, and at higher temperatures (*i.e.* several hundred degrees Celsius) the preference for Bi_2Te_3/Sb_2Te_3 systems yields to other materials including lead telluride (PbTe) and silicon germanium (SiGe), appropriately doped to achieve desirable properties. Functionalized thermoelectric devices present many additional complications which are irrelevant in metal thermocouple temperature-sensing applications. For example, in a power generating or heat pumping thermoelectric device, many alternating thermoelements must be assembled into a thermopile, or series of thermocouples, in order to benefit from series-additive electric potentials. This presents challenges in material interconnects to transport electric charge throughout the device, which introduces metal/semiconductor interfaces and (sometimes) significant electrical contact resistances. The assembly must be packaged into a mechanically-robust device, and must be coupled to the surrounding environment to absorb and dissipate heat on either side of the device. This component in particular introduces important system-level optimization considerations, as the performance of the device will be largely dictated by the quality of thermal coupling to the heat source and sink. Furthermore, the addition of heat exchangers to the design alters the formulation through additional resistance and cost considerations which may easily shift the parameters for the ideal *engineering design* away from the ideal *theoretical design*.

In this chapter, we endeavor to present a more comprehensive perspective on the analysis and design of thermoelectric power generation systems, as opposed to literature which most often focuses on a particular aspect of the system such as material properties or generator geometry without consideration for other high-impact components in the thermal pathway. Furthermore, there is little or no prior experimental work in optimizing TEG outputs relative to adjusting external thermal resistances on a TEG system because this is quite expensive and no one has really had the budget or motivation to address this experimentally. Therefore, this work and much prior work has focused on analytic models to bound the optimization problem for specific designs, analyze specific cases, or otherwise apply design-specific

boundary conditions appropriate to a given application or project. TEG systems have been investigated and applied to some automotive applications in U.S. Department of Energy projects, where optimized systems were attempted, but significantly underachieved, due thermal interface issues and hot-side and cold-side thermal resistances that were not properly optimized or design conditions were not solidly specified due to unknown transients [1–4]. TEG systems have been proposed in industrial waste heat recovery [5], but never implemented because cost and performance optimized systems have not been attainable to date, in part because designers and design work did not focus properly on hot- and cold-side thermal resistance optimization as discussed extensively herein. A comprehensive performance analysis completely encompassing the combined effects of hot- and cold-side thermal resistances, such as performed and described herein, is required to begin to address the requirements on hot- and cold-side thermal design to optimize TEG systems. This treatment illustrates thermoelectric power generation systems as highly-coupled, inter-disciplinary devices which will be best applied in real-world engineering applications when the multi-scale contributions of the system from nanoscale energy carrier transport all the way to ambient heat exchangers are considered. To lay the groundwork for the analyses in this chapter, we begin with an overview of the primary thermoelectric phenomena and their significance in developing a functional thermoelectric device.

1.1 The Seebeck effect

In the presence of a temperature gradient, carriers such as phonons (matter waves which carry thermal energy through the lattice), free electrons, or free holes will transport thermal energy from the hot end of a material to the cold end through diffusion mechanisms. When diffusion of free electrons and holes occurs, an electric potential will also be established across the material as the population density of charge carriers increases at the cold end, which is sustained by the thermal energy diffusion. Depending on the majority electric charge carrier of the material (electrons in n-type semiconductors and holes in p-type semiconductors), either a positive or negative voltage potential will be present along the thermal gradient as illustrated in Fig. 1, which is representative of parallel thermoelements in electrical isolation from each other.

The Seebeck voltage is the electromotive force reacting to the buildup of charged carriers in the material and is defined mathematically as the product of the temperature gradient ∇T and the Seebeck coefficient S:

$$E_{emf} = -S\nabla T \tag{1}$$

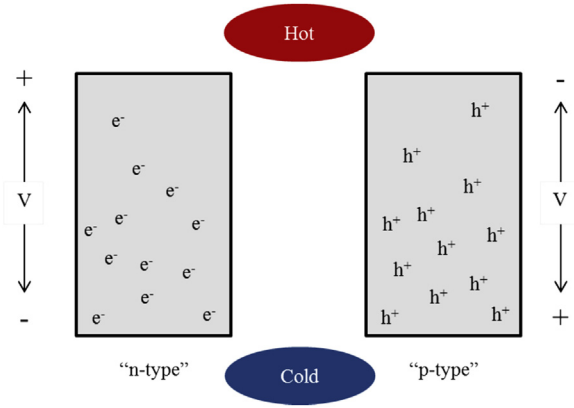

Fig. 1 Illustration of the Seebeck effect in n- and p-type thermoelectric materials.

This term contributes to the electric current density J, such that:

$$J = \sigma\left(-\nabla V + E_{emf} \right) \tag{2}$$

In the absence of electric current flow through the material (*i.e.* open-circuit), the Seebeck coefficient can be defined, and measured, as the negative ratio of the local voltage and temperature gradients:

$$S = -\frac{\nabla V}{\nabla T} \tag{3}$$

Eq. (3) is valid for zero current flow through the material and for small temperature gradients, as the Seebeck coefficient is in general a temperature-dependent property. In semiconductors exhibiting strong thermoelectric properties, the Seebeck coefficient of a p-type material will have positive polarity, while the Seebeck coefficient of an n-type material will have a negative polarity. In the nominal Bi_2Te_3/Sb_2Te_3 thermoelectric system, Bi_2Te_3 is an n-type material and typically exhibits a Seebeck coefficient value near room temperature of -200 to -220 $\mu V\ K^{-1}$, while Sb_2Te_3 is a p-type material with a typical room temperature Seebeck coefficient near $+170\ \mu V\ K^{-1}$.

1.2 The Peltier effect

When electric current is passed through a thermoelectric material, heat, in addition to electric charge, is transported by the diffusion of the charge carriers. If two dissimilar materials, such as those illustrated in Fig. 1, are brought into electrical contact, a junction forms at the interface. When the electric current passes through this junction, a discontinuity in heat flow driven by the electric current arises due to the change in local Seebeck coefficient, and heat is either absorbed or rejected at the interface as a result of the

requirement for energy conservation. This phenomenon is referred to as the Peltier effect, and with conventional current flowing from material 1 to material 2, is described mathematically as:

$$\dot{Q}_{Peltier} = (S_1 T_1 - S_2 T_2) I_{1\to 2} \tag{4}$$

where T_1 and S_1 are the local temperature and Seebeck coefficient of material 1 at the interface, T_2 and T_2 are the local temperature and Seebeck coefficient of material 2 at the interface, and $I_{1\to 2}$ is the current passing through the junction from material 1 to material 2. In a thermoelectric device, this phenomenon typically occurs at the interface of one of the thermoelements and an interconnect material used to electrically connect the p-type and n-type materials. The interconnect materials are typically made of a conductive metal such as copper or gold, which exhibits a large electrical conductivity and a low Seebeck coefficient. The effect is illustrated in Fig. 2 for a single thermocouple of an n-type material ($S_n < 0$), a p-type material ($S_p > 0$), and a metallic interconnect ($S \sim 0$).

With the direction of electric current flowing from n-type to p-type material after the standard convention of following the positive charge carriers, the heat rate described in Eq. (4) is negative at the top of Fig. 2 ($\dot{Q} = (S_n - 0)TI^+$ and $\dot{Q} = (0 - S_p)TI^+$), indicating that heat is absorbed at the junctions as illustrated in the figure. In a device designed as a heat pump, this end would be placed in thermal contact with a heat source requiring thermal energy removal, such as a high heat-flux electronic component or the interior of a refrigerated cavity. Conversely, the heat rate is positive at the interfaces at the bottom of Fig. 2 ($\dot{Q} = (0 - S_n)TI^+$ and $\dot{Q} = (S_p - 0)TI^+$), indicating that heat is rejected or released at the junctions. In the heat pump system, this end would be connected to a heat sink which would dissipate thermal energy to ambient, typically through natural or forced convection. In this manner, the thermocouple

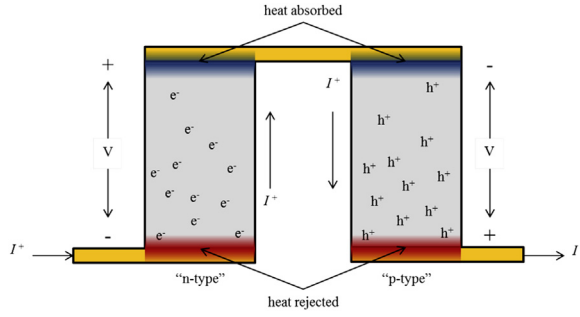

Fig. 2 Illustration of the Peltier effect in a thermocouple structure.

acts as a heat pump from top to bottom in the figure. Changing the direction of electric current likewise reverses the direction of heat pumping, which also permits the use of these devices in systems requiring active thermal control with a feedback design, as it is able to supply heat to or remove heat from one side with just a flip in polarity of the connected current source.

1.3 The Thomson effect

When a temperature gradient is present which results in variation of the temperature-dependent Seebeck coefficient, electric current passing through the material will cause the release or absorption of a continuous differential amount of heat along the current pathway inside the material to preserve energy conservation. This heat arises from the Thomson effect, which in essence is the Peltier effect inside a single material due to differential changes in the local Seebeck coefficient, taking the form:

$$\dot{Q}_{Thomson} = -I\frac{dS}{dT}T \tag{5}$$

In the Thomson heat relation, the change in Seebeck coefficient across a local thermal gradient acts as the "dissimilar junction" which gives rise to the Peltier effect described in Eq. (4).

1.4 Use of thermoelectric phenomena in functional devices

The thermoelectric phenomena described in Sections 1.1-1.3, most significantly the Seebeck and Peltier effects, lend themselves to convenient use for solid-state thermal management and electric power generation. Such devices offer distinct benefits to traditional working fluid-driven thermodynamic systems, in their ability to provide a compact solution with no moving parts. Here we outline the basic structure and functionality in assembled thermoelectric device architectures.

1.4.1 Thermoelectric devices for thermal management

Thermoelectric devices enjoy relatively widespread use as thermal management solutions for systems requiring active heating and cooling, with applications including refrigerators [6], vehicle seat temperature controllers [7], coolers for microelectronics [8], and more. While typically demonstrating a lower coefficient of performance than traditional thermodynamic heat pumps and refrigeration cycles, advantages exist in their rapid response time and the fact that they are solid state devices with no moving parts [6]. Thermoelectric devices used in this manner rely fundamentally on the Peltier effect, described in Section 1.2. By arranging a large number of thermocouples thermally in parallel and electrically in series as illustrated in Fig. 3, a driving current will

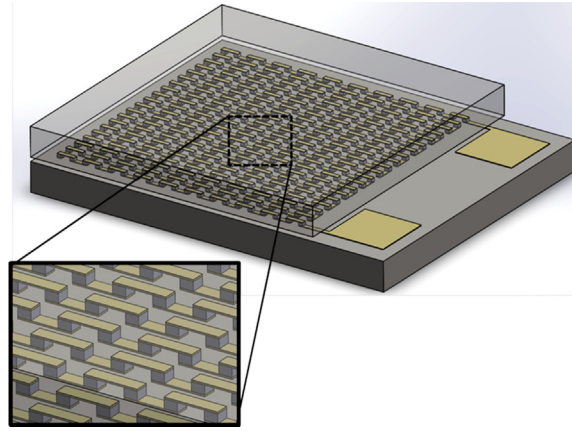

Fig. 3 Illustration of vertically-aligned Peltier device with thermoelectric elements arranged thermally in parallel and electrically in series. In this design, current would be supplied using the protruding square contact pads and heat would be pumped up or down through the device, depending on the direction of electric current.

pump heat from one side of the device to the other via heat absorption or rejection at each material junction according to Eq. (4).

The magnitude of heat released or absorbed at each junction is proportional to the transmitted electric current, and to a point an increase in electric current drives more heat through the device by the Peltier effect. However, the materials in a Peltier device are not perfect conductors, and resistive Joule heating enters the heat balance proportional to the square of current as:

$$\dot{Q}_{Joule} = I^2 R \tag{6}$$

This competing term dominates with sufficiently high currents in a Peltier device, resulting in an optimal cooling condition, after which point Joule heating will dominate and release heat throughout the entire device.

1.4.2 Thermoelectric devices for electric power generation

Though Peltier devices for thermal management have comprised the bulk of the thermoelectrics market for many years, devices for power generation are receiving increased interest in a variety of applications beyond legacy spacecraft power generation in recent years. The remainder of this chapter will focus on the configuration used to convert thermal energy to electricity, known as a thermoelectric generator (TEG), and various factors illustrating the complexity of optimizing the power transfer in a highly-interconnected engineering system. For electric power generation, thermoelectric devices make use of the Seebeck effect described in Section 1.1. Like thermal management devices such as Peltier coolers/heaters, thermoelectric generators

are most commonly designed with thermoelements which are arranged thermally in parallel and electrically in series, as in Fig. 3. By connecting a large number of thermocouples in this manner, the electric potential produced by the Seebeck effect is linearly related to the thermocouple count n_{TC} as given in Eq. (7):

$$V_{Seebeck} = n_{TC} S_{net} \Delta T_{TE} \tag{7}$$

When the circuit is closed with an electric load, power is transferred at a magnitude that varies with the ratio of electrical resistance of the TEG to the electrical resistance of the connected load. In the absence of the Peltier and Thomson effects and losses like Joule heating and contact resistances, standard power transfer theory holds and the maximum power point occurs when the electrical resistance of the load matches the electrical resistance of the TEG. This requires either the use of a power management and maximum power point tracking (MPPT) system in addition to the TEG, or the ability to design the TEG to have an electrical resistance appropriately matched to the load for maximum power transfer. The inclusion of thermoelectric-specific phenomena, most specifically the Peltier effect, and device-level losses causes a deviation from this design point unique to thermoelectrics, and will be discussed in more detail in Section 2. In addition to electrical load matching, an ideal TEG operating between heat source and heat sink thermal reservoirs will produce the most electric power when its internal thermal resistance is designed to be matched to the sum of the hot-side and cold-side thermal resistance of the external heat exchangers. For example, if a TEG is to operate between a heat source of 200°C and a sink of 100°C, and two heat exchangers are used which total 10 K W^{-1} thermal resistance to couple the TEG to the reservoirs, theory indicates that the TEG should be designed to provide 10 K W^{-1} of thermal resistance in the system, resulting in 50°C temperature difference across the TEG and a 50°C temperature difference in total exterior to the TEG. This is a somewhat peculiar consequence which has sparked notable debate in the scientific community, and can be a difficult concept to accept for scholars new to thermoelectrics. We dig more deeply into these design criteria and their consequences in Section 2.

In an effort to promote the utilization of thermoelectric devices and TEGS in particular, there have been many examples in the literature focused on the optimization of TEGs through various means. Geometric design choices [9–11], such as the arrangement of thermocouples, the cross-sectional dimensions of the individual thermoelements, the aspect ratio of the thermoelements, and even unique thermocouple orientation such as

horizontal structures deviating from the typical vertical structure shown in Fig. 3 represent means of geometric optimization which are typically used to design a device to have a desirable combination of electrical and thermal resistance for a given application. Beyond geometric device design, ubiquitous efforts have been demonstrated to improve thermoelectric device performance through enhanced material properties [56], which include development of new materials, optimized processing techniques to achieve desired microscopic grain structures, selective doping and defect engineering for targeted carrier scattering or transport enhancement, and nanoengineering to manipulate the fundamental carrier transport.

Less scrutiny has generally been applied to the importance of the hot-side and cold-side thermal design (*i.e.*, heat exchangers) in optimizing thermoelectric generator (TEG) performance, which has been discussed as far back as 2002 [12] but is often critically misunderstood. These external thermal resistances are the coupling mechanisms between the thermal reservoirs driving heat transfer into and out of the TEG, and determine the fraction of temperature drop available to the TEG for useful energy conversion (*i.e.* the ΔT_{TE} term in Eq. 7). When taking a system-level design approach, it is apparent that these components significantly impact the optimal design choices for the TEG itself, and must be properly accounted for in the overall TEG thermal network. Various studies have demonstrated [11–17] that these external thermal impedances (including heat exchanger effects) impact and in many ways govern the power output, thermal performance, mass and volume of the TEG system. More recently Hendricks [18] further demonstrated that the hot-side and cold-side heat exchanger in the TEG design also control and govern the cost of TEG systems in terrestrial energy recovery applications. There has been much discussion in the thermoelectric design community regarding how to properly design, target, and select TEG hot- and cold-side thermal resistances to maximize TEG power output. In addition to standard TEG-level optimization approaches, we will discuss the interplay and interdependencies between the hot- and cold-side thermal resistances and the temperature-dependent thermoelectric (TE) properties in optimizing the TEG design. This treatment provides new insights and design guidance for TEG systems that challenge contemporary design logic. Past TEG design work has intuitively drawn attention to this topic and accounted for it informally in the design process as temperature-dependency of TE properties has long been accounted for in TEG designs. The more formal, systematic approach presented here serves to provide a deeper understanding and insight into the interdependencies and relationships between the hot- and cold-side thermal resistances, the temperature-

dependent thermoelectric (TE) properties in optimizing the TEG design, and the exergy capture within the TEG system. We then extend upon these findings to draw conclusions about the implications for nano-engineering of thermoelectric materials and cost optimization associated with TEG system design.

2. Analytical TEG models and impedance matching concepts

To support reader's fundamental understanding of TEG operation, the electro-thermal coupling mechanisms which drive system design, and to lay the groundwork for the more complex analyses presented in Sections 3–5, we begin with a review of the derivation of common analytical TEG models and optimization conditions. A simple model with reasonable accuracy for devices in which the heat flow can be assumed to be approximately one-dimensional involves a coupled set of equations representing thermal and electrical resistor networks. This primarily applies to the classic vertical structure illustrated in Fig. 3, as the regular, parallel arrangement of thermoelements surrounded by a thermally-insulating medium (*e.g.* air, vacuum, aerogel, or other thermal insulation materials) is generally well-represented by a 1D analysis. The representative thermal and electrical networks are illustrated in a nodal heat balance for the thermal system and a linear circuit for the electrical system in Fig. 4 [11–13].

Most often the thermal resistances for the thermoelements and the surrounding filler material in the network shown in Fig. 4A are calculated as 1D

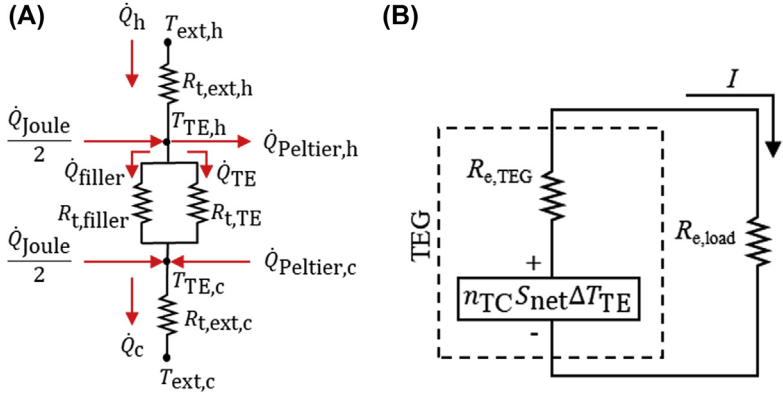

Fig. 4 Illustration of common (A) thermal and (B) electrical resistor networks for 1D analysis of electro-thermally coupled thermoelectric generators.

thermal resistance values based on the medium's length l in the direction of heat flow, the medium's thermal conductivity k, and the cross-sectional area A of the medium normal to the direction of heat flow:

$$R_t = \frac{l}{kA} \tag{8}$$

If the system cannot be accurately represented in the 1D heat flow regime, for example when the fraction of cross-sectional area of thermoelectric elements over the total cross-sectional area (also known as the fill fraction or fill factor) is very small, thermal spreading and constriction resistances into and out of the thermoelement array can sometimes be accounted for with modified geometric factors [19]. In Fig. 4A, the hot and cold side thermal resistances, $R_{t,h}$ and $R_{t,c}$ respectively, represent the total thermal resistance between the thermocouple junction and the reservoir on either side. Typically this includes an electrically-insulating substrate (*e.g.* Al_2O_3, AlN, or Si), a structure to transfer heat to/from the reservoir via conduction, convection, and/or radiation, and any thermal contact resistances at interfaces between components and materials.

The electrical system is always coupled to the thermal system, as the induced Seebeck voltage in the circuit is proportional to the number of thermocouples n_{TC}, the net Seebeck coefficient S_{net} of one of the repeating thermocouples, and the temperature gradient across the thermoelements ΔT_{TE} (not including temperature drop across materials and media not contributing significantly to the Seebeck effect, such as interconnects, interfaces, and substrates):

$$V_{Seebeck} = n_{TC} S_{net} \Delta T_{TE} \tag{9}$$

The electric current in the TEG-load system is then determined by the induced Seebeck voltage and the series resistance of the generator $R_{e,TEG}$ and the load $R_{e,load}$ through Ohm's law:

$$I = \frac{n_{TC} S_{net} \Delta T_{TE}}{R_{e,TEG} + R_{e,load}} \tag{10}$$

If Peltier, Joule, and Thomson heat contributions are accounted for, then the thermal system is likewise coupled to the electrical system through the current I in these terms:

$$\dot{Q}_{Peltier} = n_{TC} I S_{net} T \tag{11}$$

$$\dot{Q}_{Joule} = I^2 R_{e,TEG} \tag{12}$$

$$\dot{Q}_{Thomson} = -n_{TC} I \frac{dS}{dT} T \tag{13}$$

With the assumption of temperature-independent properties, common in many design analyses and usually accurate for TEG systems operating with temperature gradients of a few tens of °C or less, dS/dT and subsequently the Thomson heat are equal to zero. The heat rate balances use the analog of Kirchoff's current law to heat transfer, and with temperature-independent properties become:

$$\begin{aligned} 0 &= -\dot{Q}_h + \dot{Q}_{TE} + \dot{Q}_{filler} + \dot{Q}_{Peltier,h} - \frac{\dot{Q}_{Joule}}{2} \\ &= -\frac{T_{ext,h} - T_{TE,h}}{R_{t,h}} + \frac{T_{TE,h} - T_{TE,c}}{R_{t,TE}} + \dot{Q}_{filler} + n_{TC} S_{net} T_{TE,h} I \\ &\quad - \frac{I^2 R_{e,TEG}}{2} \end{aligned} \tag{14}$$

$$\begin{aligned} 0 &= \dot{Q}_c - \dot{Q}_{TE} - \dot{Q}_{filler} - \dot{Q}_{Peltier,c} - \frac{\dot{Q}_{Joule}}{2} \\ &= \frac{T_{TE,c} - T_{ext,c}}{R_{t,c}} - \frac{T_{TE,h} - T_{TE,c}}{R_{t,TE}} - \dot{Q}_{filler} - n_{TC} S_{net} T_{TE,c} I - \frac{I^2 R_{e,TEG}}{2} \end{aligned} \tag{15}$$

The concept of "load matching" alluded to earlier is ubiquitous in the thermoelectrics literature and discussed in more detail here. This term can have three distinct meanings: (1) the matching of electric resistance of the load and the electrical resistance of the TEG, (2) matching of the thermal resistance of the "internal" or "active" thermoelectric region of the system (*i.e.* the thermal resistance of the parallel array of thermoelements) and all "external" thermal resistances (*i.e.* interfaces, interconnects, substrates, and external heat exchangers), and (3) matching, or more appropriately, "balancing," of the thermal resistances exterior to the active region (*e.g.* the heat coupler and heat sink resistances) on the hot and cold side of the generator with one another. We will review each of these concepts here for completeness, accompanied by the illustrations in Fig. 5.

2.1 Electrical impedance matching

Electrical impedance matching for TEGs follows the principle of maximum power transfer conditions in a resistive circuit. For a real power source with non-zero internal resistance $R_{e,TEG}$ the voltage and current developed across a load $R_{e,load}$, and subsequently the power transferred to the load, will vary

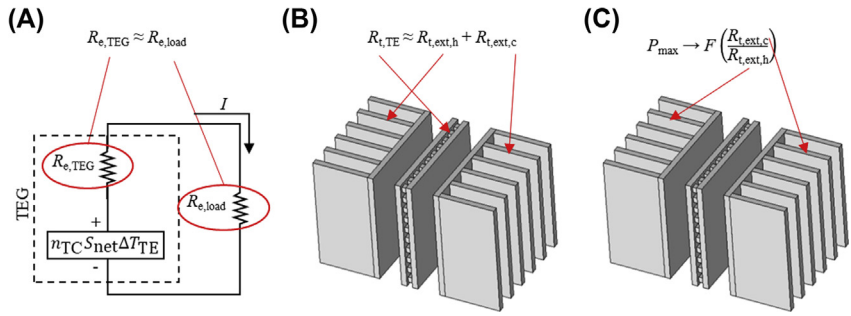

Fig. 5 Illustrations for three types of impedance matching concepts: (A) Electrical impedance matching, (B) Internal/external thermal impedance matching, and (C) External/external thermal impedance matching.

with the ratio of the load resistance to the source resistance. It is easily derivable that for such a circuit with constant properties and constant hot-side and cold-side temperatures, the maximum power transfer occurs when $R_{e,load} = R_{e,TEG}$ (see Fig. 5A).

$$P_{load} = \frac{{V_{load}}^2}{R_{e,load}} = \frac{\left(n_{TC}S_{net}\Delta T_{TE} \times \frac{R_{e,load}}{R_{e,TEG}+R_{e,load}}\right)^2}{R_{e,load}} \tag{16}$$

$$\begin{aligned}\frac{dP_{load}}{dR_{e,load}} &= \frac{d}{dR_{e,load}}\left[\frac{\left(n_{TC}S_{net}\Delta T_{TE} \times \frac{R_{e,load}}{R_{e,TEG}+R_{e,load}}\right)^2}{R_{e,load}}\right] \\ &= -\frac{\left(n_{TC}S_{net}\Delta T_{TE}\right)^2\left(R_{e,load} - R_{e,TEG}\right)}{\left(R_{e,TEG} + R_{e,load}\right)^3}\end{aligned} \tag{17}$$

In most simplified analyses this principle is utilized to match the electrical resistance of the load to the electrical resistance of the TEG for assumed maximum power transfer. A deviation occurs when Peltier heating at the thermocouple junctions is considered. The maximum efficiency, or in cases of constant heat load maximum efficiency and maximum power transfer, condition can be derived with some simplifications to be at a load resistance proportional to a factor $m_{max\text{-}efficiency}$ [8,53], where:

$$m_{max-efficiency} = \sqrt{1 + ZT} \tag{18}$$

and ZT is the average thermoelectric material figure of merit, which essentially accounts for the Peltier effect and complicates the thermal and electrical co-optimization,

$$ZT = \frac{S^2\sigma}{k}T \tag{19}$$

In most cases the point of maximum efficiency and maximum power transfer do not precisely coincide, and the maximum power transfer is found at a different $m_{max\text{-}power}$ value, which is also larger than unity. The maximum power expression then becomes:

$$P_{max} = \frac{\left(n_{TC}S_{net}\Delta T_{TE}\right)^2}{\left(m_{max\text{-}power}\cdot R_{e,TEG} + R_{e,TEG}\right)^2}\cdot m_{max\text{-}power}\cdot R_{e,TEG} \tag{20}$$

In the ZT relation, S is the Seebeck coefficient (V K^{-1}), σ is the electrical conductivity (Ω^{-1}), k is the thermal conductivity (W m^{-1} K^{-1}), and T is the average temperature of the thermoelectric material. The Peltier effect causes the maximum power point condition to always occur for an electrical load resistance which is greater than the electrical resistance of the TEG. This shift is illustrated in Fig. 6, and conceptually is due to the heat pumping action of the Peltier effect causing a *reduction* in temperature gradient ΔT_{TE} seen by the TEG. It is then beneficial to extend the length of the thermoelements to capture additional ΔT due to increased thermal resistance. This design choice also increases the electrical resistance of the TEG.

In more analytical terms: when hot-side and cold-side temperatures of the TE material are not held constant and power generation occurs in a system with constant external temperatures (*i.e.*, external ambient

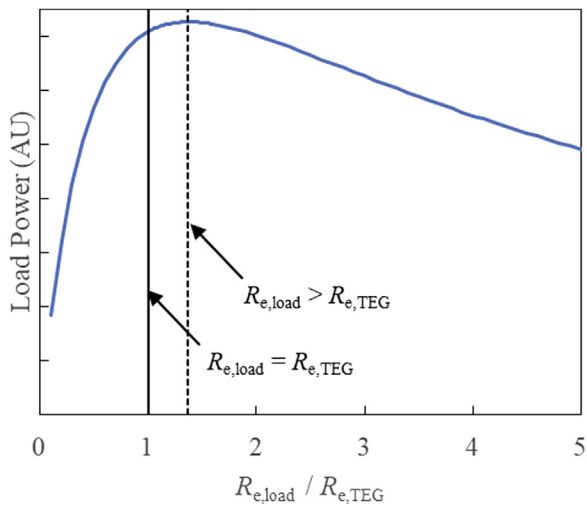

Fig. 6 Load power versus load-to-TEG electrical resistance ratio, showing the sub-optimal outcome for direct electrical load matching.

temperatures, T_{source} and $T_{ambient}$) as is common in energy recovery applications, the maximum power transfer occurs at a resistance $R_{e,load} > R_{e,TEG}$ because the presence of variable hot-side and cold-side temperatures as $R_{e,load}$ varies creates an additional dT/dR term in Eq. (17), as shown in Eq. (21), which results in an additional Peltier contribution. The strength of the Peltier contribution is proportional to the electric current, so while increasing the total series resistance decreases the power transfer to the load, it also decreases the strength of the Peltier heat contribution. In addition, the choices which increase the electrical resistance, typically increasing the length of the thermoelements or decreasing their cross-sectional area, also increase the thermal resistance of the TEG, resulting in a larger ΔT_{TE}. The realistic maximum power transfer condition of $R_{e,load} \neq R_{e,TEG}$ significantly complicates the optimization procedure, as it requires a multi-parameter optimization along with the thermal resistance, and is generally addressed by utilizing Eq. (18). More precisely, when considering the power output from the TEG module given by Eq. (16): the traditional $R_{e,load} = R_{e,TEG}$ peak power condition occurs when this equation is differentiated with respect to $R_{e,TEG}$ and set to zero assuming fixed $R_{e,load}$ and constant ΔT_{TE}. However, to determine the peak power condition in the system-level analysis, ΔT_{TE} must be assumed variable, largely due to the electro-thermal coupling via the Peltier effect, and the differentiation then becomes more complex. The peak power condition is then:

$$R_{e,load} = R_{e,TEG} + \frac{2R_{e,load}R_{e,TEG} + 2R_{e,load}^2}{\Delta T_{TE}} \frac{\partial(\Delta T_{TE})}{\partial R_{e,load}} \tag{21}$$

This equation shows that $R_{e,load} > R_{e,TEG}$ by an amount related to the derivative of module temperature differential with respect to $R_{e,load}$, and is therefore related to the module temperature differential dependence on $R_{e,load}$. This equation results in a quadratic relationship for $R_{e,load}$ to explicitly quantify the $R_{e,load} > R_{e,TEG}$ peak power condition in any particular system-level analysis.

2.2 Internal/external thermal impedance matching

Matching of internal and external thermal impedances in TEGs refers to the concept of matching the thermal resistance of the internal active region (*i.e.* the parallel array of thermoelements) with the total sum of thermal resistance between the external thermal reservoirs and the active region (see Fig. 5B).

The effect of this matching is that half of the available temperature difference is developed across the thermoelements for the assumption of temperature-independent TE properties. For example, if the TEG is to operate between a source of 200 °C and sink of 100 °C, this principle states that the maximum power generation will be realized when the TEG is designed such that the thermoelements see a temperature gradient of 50 °C. Since the mechanisms for increasing TEG thermal resistance (which increase ΔT_{TE} and the developed voltage) also increase electrical resistance (which increases $R_{e,TEG}$ and decreases the developed current and power), an optimum condition exists where it becomes detrimental to further increase the share of total ΔT across the thermoelements. This seems counter-intuitive out of context, as by examination of the load power expression in Eq. (20) it appears that the module should be designed to achieve the maximum ΔT_{TE} possible. We prove the thermal load matching relation for the ideal TEG beginning with the expression for power output given by Eq. (20). By neglecting Peltier, Joule, and Thomson heating effects we can then express the temperature gradient across the active thermoelectric region, ΔT_{TE}, in terms of the thermal resistance of the thermoelectric region (*i.e.* the internal thermal resistance) $R_{t,TE}$, the external thermal resistance (*i.e.* the sum of hot and cold side heat exchangers, etc.), and the total available reservoir temperature gradient ΔT_{ext}. These assumptions decouple the thermal system model from the electrical system model through the Peltier, Joule, and Thomson effects, while the coupling of the electrical system to the thermal system through the Seebeck effect is retained.

$$P_{load} = \frac{\left(n_{TC} S_{net} \Delta T_{TE}\right)^2}{\left(R_{e,TEG} + R_{e,load}\right)^2} R_{e,load} = \frac{R_{e,load} n_{TC}^2 S_{net}^2}{R_{e,TEG}^2 + 2R_{e,TEG} R_{e,load} + R_{e,load}^2} \times \frac{R_{t,TE}^2 \Delta T_{ext}^2}{R_{t,TE}^2 + 2R_{t,TE} R_{t,ext} + R_{t,ext}^2} \tag{22}$$

The electrical resistance of the thermoelectric, $R_{e,TEG}$, is coupled to the thermal resistance, $R_{t,TE}$, through the thermoelement length l and/or the thermoelement cross-section A_{TE}. We can write the thermoelement length l in terms of the thermal resistance as:

$$l = 2 n_{TC} k A_{TE} R_{t,TE} \tag{23}$$

and subsequently the TEG electrical resistance as:

$$R_{e,TEG} = 4n_{TC}^2 \rho_{TE} k R_{t,TE} \tag{24}$$

Substituting Eq. (24) into Eq. (22), we obtain the following relation for load power:

$$P_{load} = \frac{R_{e,load} n_{TC}^2 S_{net}^2}{16 n_{TC}^4 \rho_{TE}^2 k^2 R_{t,TE}^2 + 16 n_{TC}^2 \rho_{TE} k R_{t,TE} R_{e,load} + R_{e,load}^2} \times \frac{R_{t,TE}^2 \Delta T_{ext}^2}{R_{t,TE}^2 + 2 R_{t,TE} R_{t,ext} + R_{t,ext}^2} \tag{25}$$

If we then take the derivative of Eq. (25) with respect to the internal thermal resistance $R_{t,TE}$ and substitute Eq. (24) back in, we obtain:

$$\frac{dP_{load}}{dR_{t,TE}} = -\frac{S_{net}^2 \Delta T_{ext}^2 \left(R_{t,TE} - R_{t,ext}\right)}{24 k \rho_{TE} \left(R_{t,TE} + R_{t,ext}\right)^3} \tag{26}$$

The derivation resulting in Eq. (26) shows that, in the absence of accounting for Peltier, Joule, and Thomson heating effects in the second product term of Eq. (25) for calculating the temperature gradient across the active thermoelement region, the load power from a TEG will be optimized $\left(\frac{dP_{load}}{dR_{t,TE}} = 0\right)$ when the geometry is designed such that the internal thermal resistance of the active thermoelement array matches the sum of all external, or inactive, thermal resistance contributions. This concept is commonly used as a design criterion in the literature [20], although several works have noted that the actual optimum ratio can vary depending on various factors, including filler material, contact resistances, interconnects, etc. [11,12]. The calculated TEG thermal resistance is larger than the sum of external resistances when the Peltier effect is included due to the fact that the Peltier heat reduces ΔT_{TE}, which effectively reduces the apparent thermal resistance of the TEG. The factor by which it reduces the apparent TEG resistance is determined by the figure of merit ZT. These concepts are illustrated in Fig. 7.

The internal/external thermal resistance matching criterion must be utilized with caution, as nonlinear deviations from temperature-dependent properties and the increased strength of the Peltier effect across large

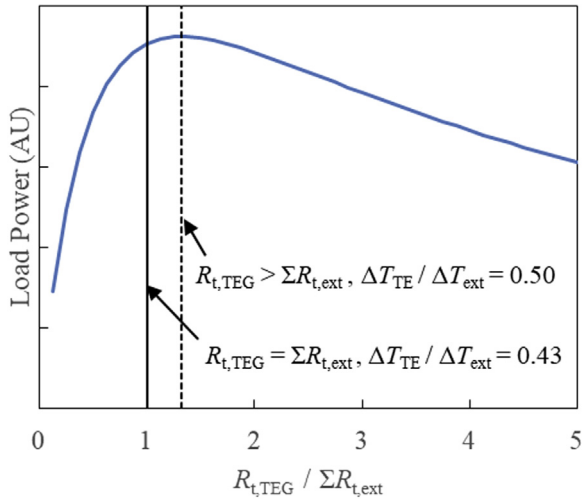

Fig. 7 Load power versus TEG-to-total external thermal resistance ratio, showing the sub-optimal outcome for direct thermal load matching when the Peltier effect is included.

temperature gradients often lead to significant error with this assumption. Significant errors can also arise in microscale geometries where electrical losses due to contact resistances and interconnects may become very significant.

We note that the general process for optimization of the ratio of thermal resistances should be followed by first determining the total sum of external thermal resistance. Then the TEG should be designed such that half the total available temperature drop from heat source to heat sink will be dropped across the thermoelements with the Peltier effect accounted for. Reducing the external thermal resistances after achieving this design condition will increase the load power due to the resulting increase in ΔT_{TE} in Eq. (16). However, in this situation, this is no longer the optimal design. Reducing the TEG thermal resistance to again reach the condition of $\Delta T_{TE} = ½ \Delta T_{ext}$ will further increase load power by reducing electrical resistance from this point. While it is counter-intuitive that reducing ΔT_{TE} would *increase* load power, it is by the mechanism used to reduce the thermal resistance (*e.g.* shortening thermoelement length or increasing cross-sectional area) which simultaneously reduces the electrical resistance, leading to the increase in load current and power.

2.3 External/external thermal impedance matching

Matching, or "balancing," of external thermal impedances in TEG systems is a far less-discussed topic of optimization, first proposed by Hendricks [15] who noted a dependence of maximum power delivered to a load on the ratio of hot side to cold side external thermal resistance (see Fig. 5C). Hendricks found that the ratio of hot-side external thermal resistance to cold-side external thermal resistance $R_{t,ext,h}/R_{t,ext,c}$ in specific case studies should be $> 10-30$ to maximize power output because of its strong impact on ΔT across the TE devices. When additional loss mechanisms and, most importantly, temperature-dependence of the TEG materials are considered in the analysis, the balancing of thermal resistances on the hot and cold side of the TEG can be significant in the maximizing of power output. Since inclusion of temperature-dependence in material definitions effectively requires computationally-expensive finite element modeling and knowledge of the temperature-dependency of specific TE material properties, it is not commonly utilized or discussed in the literature. Furthermore, while it is well-known that the material thermoelectric figure of merit Z is strongly temperature-dependent, it does not seem to be generally appreciated that this also means that this strong temperature-dependence propagates into system-level optimization. Our presentation of more detailed analyses of TEG systems beyond the simplified resistor network systems discussed to this point enables a comprehensive examination of how effects such as Peltier heat and temperature-dependent material properties influence the proper design of TEG systems.

3. Finite element simulations of thermocouples with temperature-independent properties

COMSOL™ Multiphysics is an example of a Finite Element Analysis (FEA) tool commonly used to model complex multiphysics systems, and enables us to examine and explore the interdependencies discussed above in TEG power optimization for general thermoelectric energy recovery applications. COMSOL™ models were used to perform finite element simulations of a half unit cell with periodic boundary conditions and symmetry plane to simulate an array of thermocouples, a common configuration for TE power converters. The unit cell approach enables a reduction in computation time by taking advantage of geometric symmetry in the regular array of thermocouples. For all cases, fill fraction is fixed to 0.2, meaning that in a

given unit cell 20% of the cross-sectional area is occupied by thermoelement materials and 80% is occupied by an electrically- and thermally-insulating filler material. The width of each square thermoelement is fixed at 2 mm, which is representative of commercially-available bulk-assembled thermoelectric modules. The height of the thermoelements and the connected load resistance are left as optimization parameters. The thermocouple junctions are formed by rectangular copper interconnects, flush to the sides of the thermoelements with a thickness of 500 μm. The substrates are 1 mm-thick Al_2O_3 plates. The total external thermal resistance $R_{t,ext} = R_{t,ext,h} + R_{t,ext,c}$ is assumed to be 50 K W^{-1} per thermocouple unit cell and is implemented as a convective heat transfer coefficient on the outer Al_2O_3 substrate faces where $h_{ext,h} = (R_{t,ext,h} \times A_h)^{-1}$ and $h_{ext,c} = (R_{t,ext,c} \times A_c)^{-1}$. We note that the fixed value of $R_{t,ext}$ does not include the additional thermal resistance due to the Al_2O_3 substrates, and therefore the sum of all thermal resistances external to the thermoelements is slightly larger than 50 K W^{-1}. A low-conductivity, convection- and radiation-impeding filler material (*e.g.* aerogel) is assumed with constant thermal conductivity of 0.01 W m^{-1} K^{-1}. Adding temperature-dependence to the thermal conductivity of the filler material for values representative of aerogel, for which the thermal conductivity *increases* with increasing temperature, had a negligible impact on our simulations (<2% change in max power and <0.5% change in optimum $\Delta T_{TE}/\Delta T_{ext}$ for high-temperature SiGe cases with no change in the general trends). For the assumption of constant thermoelectric properties, we initially used values comparable to Bismuth/Antimony Telluride thermocouples near room temperature, where: $S_{net} = 400\ \mu$V K^{-1}, $\sigma_p = \sigma_n = 1.5 \times 10^5\ \Omega$ m, and $k_p = k_n = 2$ W m^{-1} K^{-1}. A representative mesh of the half unit cell is shown in Fig. 8 with the filler region removed and base copper interconnects highlighted in blue for visibility.

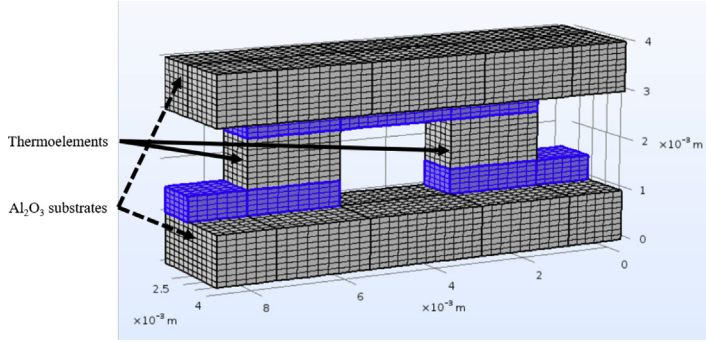

Fig. 8 Representative mesh of thermocouple structure.

Load power is calculated using the current through the variable load resistor using $P = I_{load}^2 \times R_{load}$. The electrical resistance of the thermocouple must be determined using a separate simulation in which the Peltier effect is disabled. This is due to the impact of the Peltier effect on the temperature gradient in the TEG, and therefore the Seebeck voltage which is developed. This illustrates a challenge also present in the experimental characterization of TEGs, where a device initially at room temperature will begin to develop a temperature gradient via the Peltier effect when the sense current from a multimeter is applied. This then adds a Seebeck back-EMF to the current density equation, and a non-Ohmic contribution to the resistance calculated from the measured voltage. Thus, in the simulation with the Peltier effect disabled, the voltage developed across the thermocouple is purely Ohmic and the resistance can be calculated using the known supply current. When temperature-dependent materials are examined, thermoelement junction temperatures are imported as boundary conditions from the power simulation to account for temperature-dependence of the electrical conductivity/resistivity.

In order to examine system-level effects due to various parasitic losses independent of the thermoelectric material properties, we perform a sequence of simulations beginning with Seebeck effect only (*e.g.* no Peltier, Thomson, or Joule heating are accounted for even though current is flowing) and all other system properties constant (Case 1). Of course it is physically incongruous with thermoelectric phenomena to include Seebeck and not Peltier for a power-producing device. However, as this is a common modeling and analysis assumption used to simplify systems for analytical studies, we begin with this baseline to demonstrate its limitations. We then add Peltier effects and Thomson effects (which in the case of temperature-independent material properties is zero due to constant Seebeck coefficient), and Joule heating (Case 2). Next, we add parasitic electrical losses from thermoelement/interconnect contact resistances and temperature-dependent bulk resistance in the copper interconnects (Case 3). Finally, we include temperature-dependent thermal conductivity of the alumina substrates (Case 4), defined by $k_{Alumina} = -5.5786 \times 10^{-8}\ T^3 + 1.7723 \times 10^{-4}\ T^2 - 1.9412 \times 10^{-1}\ T + 80.68\ \mathrm{W\ m^{-1}\ K^{-1}}$, fit from data in [55]. Thermoelement leg length and electrical load resistance are allowed to vary in a derivative-free optimization routine to determine the maximum load power for a range of ratios of external thermal resistance $R_{t,ext,c}/R_{t,ext,h}$. We show the resulting temperature fraction across the active thermoelectric region and load power in Fig. 9B. As the ratio $R_{t,ext,c}/R_{t,ext,h}$

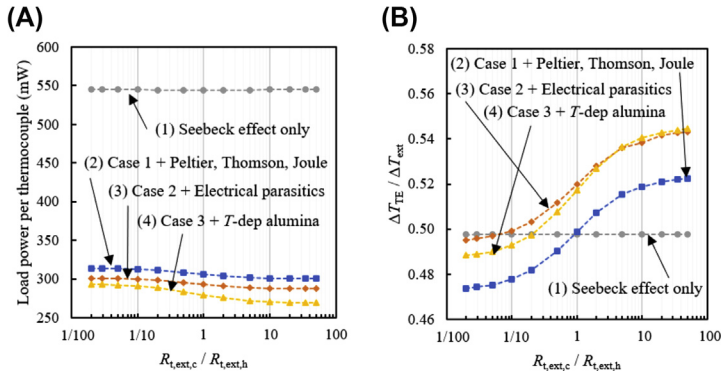

Fig. 9 (A) Maximum load power per thermocouple as a function of the ratio of external thermal resistances for various cases with temperature-independent thermoelectric material properties, and (B) corresponding fraction of available ΔT drawn across the active thermoelectric material.

increases, the effect is that more of the external temperature drop is shifted to the cold side from the hot side, resulting in an increase in the average operating temperature of the TEG. In other words, $R_{t,ext,c}/R_{t,ext,h} = 0$ means the TEG is operating at the lowest possible temperature range for the given boundary conditions (in this case 400 K at the heat sink and 800 K at the heat source), while $R_{t,ext,c}/R_{t,ext,h} = \infty$ means it operates at the highest possible temperature range.

We see from Fig. 9A and B that the system is fully temperature-independent for Case 1 with all material parameters constant and no Peltier heating, as we expect. Further, the maximum load power is delivered when half of the total available ΔT is drawn across the active thermoelectric materials, consistent with the derivation of internal/external thermal resistance matching in Section 2.2/Eq. (26). In these simulations, the ratio $\Delta T_{TE}/\Delta T_{ext}$ is slightly below 0.5 due to the presence of minor thermal parasitics from the filler material and thermal constriction/spreading from heat exiting the hot side substrate and entering the cold side substrate, respectively. In a perfectly ideal system with no thermal losses due to parallel pathways or heat spreading/constriction, (a non-realistic but common simplification assumption) this optimal ratio is exactly 0.5 as derived in Eq. (26). The introduction of (primarily) the Peltier effect in Case 2 lowers the maximum power output significantly, due to its effective transport of thermal energy from the hot junction to the cold junction which lowers the thermocouple ΔT_{TE} and the voltage and load power developed by the Seebeck effect. More interestingly, the Peltier effect introduces an observable temperature-

dependence in the system optimization even in the absence of any temperature-dependent material properties. The optimal ratio $\Delta T_{TE}/\Delta T_{ext}$ now effectively has odd-functional symmetry, equal to 0.5 when the external thermal resistances are matched ($R_{t,ext,c}/R_{t,ext,h} = 1$). When the bulk of external thermal resistance is shifted to the heat source (*i.e.*, hot) side and the average TEG operating temperature is shifted down, the optimal ratio $\Delta T_{TE}/\Delta T_{ext}$ is < 0.5, while the optimal ratio $\Delta T_{TE}/\Delta T_{ext}$ is > 0.5 when the bulk is shifted to the heat sink (*i.e.*, cold) side and the average TEG operating temperature is shifted up. The maximum load power is also greatest when all of the external resistance is shifted to the heat source side, meaning that the average TEG temperature is the lowest possible for the boundary conditions. These results are partially explained by the form of the Peltier heating terms (Eq. 11). At lower temperatures, a larger current can pass through the junctions without introducing significant losses in ΔT_{TE} due to the Peltier effect at the thermoelement/interconnect junctions. At higher temperatures, longer thermoelement lengths must be used to offset these Peltier-induced ΔT_{TE} losses as electrical resistance is increased faster than thermal resistance, thereby decreasing the current passing through the thermocouple junctions. This means the Peltier effect is "shunting" less heat from the hot side to the cold side.

For Case 3, the addition of electrical contact resistance (constant at $1 \times 10^{-10}\,\Omega\,\mathrm{m}^2$) and temperature-dependent thermal and electrical conductivity in the copper interconnects lowers the maximum load power and increases the thermoelement temperature fraction for the maximum load power condition. This is primarily due to the increase in parasitic electrical resistance, which decreases electric current. To compensate for the additional electrical losses, the optimization trends toward longer thermoelements which increases the TEG thermal resistance, capturing additional ΔT_{TE} and generating a larger Seebeck voltage. The odd-functional symmetry seen in Case 2 from the Peltier effect's additional heat transport contribution is retained. Case 4 adds temperature-dependence of the alumina substrates. As thermal conductivity in alumina decreases with temperature, the parasitic thermal resistance of the substrates increases as the operating range is shifted toward the heat source temperature. We note that with temperature-dependent alumina properties, the total external resistance varies throughout the range of $R_{t,ext,c}/R_{t,ext,h}$, since the thermal resistance of the substrates is not included in the fixed $50\,\mathrm{K\,W}^{-1}$ assumption as described previously. This causes additional losses at large $R_{t,ext,c}/R_{t,ext,h}$ values because the thermoelements must be longer (resulting in additional electrical

resistance) to balance the additional external thermal resistance. These results demonstrate that in the absence of temperature-dependent thermoelectric material properties, and even in the absence of *any* temperature-dependent material properties, system optimization introduces a temperature-dependence due to the Peltier effect which is not explicitly recognized in the literature. The observation of a functional dependence of power output and optimum $\Delta T_{TE}/\Delta T_{ext}$ ratio on the ratio of external thermal resistances $R_{t,ext,c}/R_{t,ext,h}$, fully outside the domain of the thermoelectricity physics in the thermoelement region of the TEG, is an insightful conclusion from a systems engineering perspective which calls for thoughtful consideration of the thermal design of the entire power generation system.

4. Finite element simulations of thermocouples with temperature-dependent properties

A common limitation of thermoelectric system analyses is the reliance on constant property models, in which the thermophysical properties of the system's constituent materials are assumed to be independent of temperature. This is convenient for simplified analytical formulations which promote rapid parameterization, and can have acceptable accuracy when thermal gradients in the system are limited to a few tens of °C or less. However, such assumptions can lead to significant error in larger-ΔT systems, such as industrial waste heat recovery and radioisotope-driven spacecraft applications. In reality all the relevant properties in thermoelectric materials are strongly temperature-dependent, and it is generally accepted that different materials are better suited for various applications depending on the conditions for the peak in the thermoelectric figure of merit ZT. For example, the ZT of an optimized Bi_2Te_3 thermoelement may be $\sim$1 at room temperature compared to PbTe which may be $\sim$0.3, while at 300°C those values are reversed, with $ZT_{Bi2Te3} \sim 0.3$ and $ZT_{PbTe} \sim 1$. The result is that in systems with large temperature gradients, where theoretical efficiencies are highest as predicted by Carnot and the second law of thermodynamics, the material properties which ultimately determine the efficiency of the system may vary dramatically, affecting the design of the system for optimal performance. To demonstrate this, we present simulation results in Fig. 10 for a TEG system operating between 400 and 800 K containing theoretical materials with peak Z at three different temperatures: 400 K (the sink temperature), 600 K (the average of sink and source temperatures), and 800 K (the source temperature). The thermal and electrical

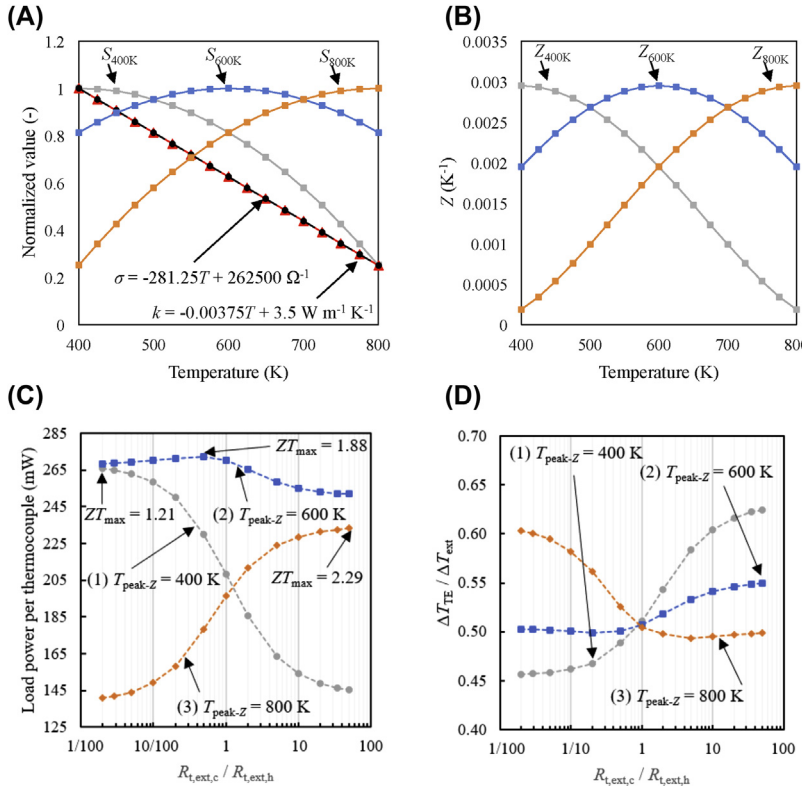

Fig. 10 (A) Normalized thermoelectric parameters for the three theoretical materials examined. Thermal and electrical conductivity functions are identical for each material, while the Seebeck curve is shifted to move the peak Z value to the desired temperature, as shown in (B). (C) Maximum load power per thermocouple as a function of the ratio of external thermal resistances for three theoretical materials having peak $Z = 0.003\ \mathrm{K}^{-1}$ at 400 K, 600 K, and 800 K, respectively, and (D) corresponding fraction of available ΔT drawn across the active thermoelectric material.

conductivities decrease linearly with temperature such that the ratio $\sigma(T)/k(T)$ is constant. The Seebeck coefficient takes three forms as a concave-down parabolic function, centered at $T_{peak\text{-}Z} = 400$ K, 600 K, and 800 K, respectively, resulting in a peak Z of $0.003\ \mathrm{K}^{-1}$ as shown in Fig. 10A and B. The functional dependence of modeled (p-type, with n-type as $S_n = -S_p$) Seebeck coefficient is $S_p = -9.2857 \times 10^{-10} \times (T - T_{peak\text{-}Z})^2 - 2.7529 \times 10^{-21} \times (T - T_{peak\text{-}Z}) + 1.9829 \times 10^{-4}\ \mathrm{V\ K}^{-1}$.

We see in Fig. 10C that the shapes of the maximum load power curves generally follow the profiles of the material Z; for a material with peak Z at 400 K, power is maximized for the lowest $R_{t,ext,c}/R_{t,ext,h}$ ratio (*i.e.* an average

TEG temperature closest to the sink temperature), while the opposite is true for the material with $T_{peak\text{-}Z} = 800$ K. In the case of peak Z at 600 K the power is still maximized for $R_{t,ext,c}/R_{t,ext,h} < 1$ where the TEG temperature is closer to the cold sink temperature, but there is a smaller power dependency between $R_{t,ext,c}/R_{t,ext,h} \sim 0.5$ and $R_{t,ext,c}/R_{t,ext,h} \sim 0.01$. The $T_{peak\text{-}Z} = 800$ K case results are dependent on the TEG system operating between 400 and 800 K and the high maximum Z at the heat source temperature. Conditions could also exist where operating at a much higher source temperature and/or lower Z values near the source temperature would shift the maximum power condition to a smaller $R_{t,ext,c}/R_{t,ext,h}$ ratio. The temperature-dependent nature of the Peltier heating thermal loss as well as the temperature-dependence of the alumina thermal conductivity is apparent in the maximum attainable load power between the $T_{peak\text{-}Z} = 400$ K and $T_{peak\text{-}Z} = 800$ K materials. More interesting to note is that for the material with peak Z at 600 K, exactly half-way between the source and sink temperatures, the peak power occurs for a $R_{t,ext,c}/R_{t,ext,h}$ ratio < 1, again due to the temperature-dependent alumina properties and Peltier effects. For each case, we calculate the maximum ZT value present in the thermoelements for the maximum load power condition and find that it is not an accurate predictor of the maximum achievable power output. In fact, the system achieving the lowest maximum power (Case 3) exhibits the highest ZT value. Larger-magnitude losses at the highest temperatures push the optimal operating range further down the Z curve toward lower temperatures and lower Z values ($1.754 \times 10^{-3}\,\mathrm{K}^{-1} \leq Z \leq 2.936 \times 10^{-3}\,\mathrm{K}^{-1}$ at maximum load power) than Case 1 ($2.002 \times 10^{-3}\,\mathrm{K}^{-1} \leq Z \leq 2.945 \times 10^{-3}\,\mathrm{K}^{-1}$ at maximum load power). These results highlight the need for careful consideration of the value of device ZT as a ranking metric for TEGs, especially when driven by larger temperature differences for high thermodynamic efficiency. We propose that an integral form of the figure of merit more accurately captures the performance potential for a system with heat source and sink defined by ($T_{ext,h}$, $T_{ext,c}$) in the form:

$$\beta = \int_{T_{ext,c}}^{T_{ext,h}} \frac{Z}{T}\, dT \tag{27}$$

This parameter effectively provides a Carnot-compensated calculation of the temperature-dependent Z profile across the minimum and maximum

temperature bounds, in essence weighing the evaluative metric toward higher-exergy systems. Calculating β for the theoretical materials considered here results in values of $\beta_{400K} = 1.360 \times 10^{-3}\,\mathrm{K}^{-1}$, $\beta_{600K} = 1.796 \times 10^{-3}\,\mathrm{K}^{-1}$, and $\beta_{800K} = 1.126 \times 10^{-3}\,\mathrm{K}^{-1}$, which correlates to the ranking of maximum optimized power produced by the different materials in this temperature range. This demonstrates the importance of the $R_{t,ext,c}/R_{t,ext,h}$ ratio, and therefore the thermal system design on the hot- and cold-side of a thermoelectric system, in determining maximum power conditions in any given application. We note that the parameter β does *not* indicate what system design conditions (*e.g.* what $R_{t,ext,c}/R_{t,ext,h}$ ratio) should be used to achieve the maximum power condition, but rather which candidate material possesses the highest output *potential* for the thermal reservoir boundary conditions. It is a combination of TE materials performance, through the material Z(T), and the hot- and cold-side thermal design, through $R_{t,ext,c}$ and $R_{t,ext,h}$ and resulting hot- and cold-side temperature conditions that dictates the maximum power achievable for any given environmental temperature difference defined by ($T_{ext,h}$, $T_{ext,c}$) because of how it influences the parameter defined by Eq. (27). The parameter β provides an insightful quantitative metric which can guide and influence thermoelectric material and thermal design decisions in any thermoelectric power system application.

In Fig. 10D we see that the fractional temperature drop $\Delta T_{TE}/\Delta T_{ext}$ converges to 0.5 at a resistance ratio of $R_{t,ext,c}/R_{t,ext,h} = 1$ for all three materials before diverging at higher and lower ratios. The trend observed is that the minimum value of fractional temperature drop $\Delta T_{TE}/\Delta T_{ext}$ occurs when the average TEG temperature approaches $T_{peak\text{-}Z}$, but ultimately at a lower value than $T_{peak\text{-}Z}$ due to the temperature-dependent losses. This explains why the curves for $T_{peak\text{-}Z} = 600$ K and 800 K present a minimum in $\Delta T_{TE}/\Delta T_{ext}$ for the evaluated boundary conditions and the curve for $T_{peak\text{-}Z} = 400$ K does not, as the minimum fraction would be present for some $T < 400$ K.

We see in Fig. 11A that the curves for TEG and load resistance in cases $T_{peak\text{-}Z} = 400$ K and 600 K follow a monotonic profile with the shift to higher average TEG temperature through increasing $R_{t,ext,c}/R_{t,ext,h}$. However, the curves for $T_{peak\text{-}Z} = 800$ K change slope from negative to positive near $R_{t,ext,c}/R_{t,ext,h} = 1$. Calculating the ratio of load to TEG electrical resistance resulting in maximum power transfer, $m_{max\text{-}power}$ plotted with solid lines/open markers in Fig. 11B, we see a more complex relationship than presented by the formula in Eq. (18). The values for $m_{max\text{-}efficiency}$ calculated

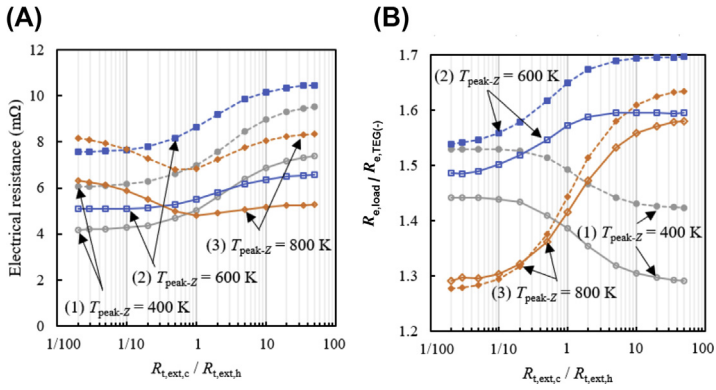

Fig. 11 (A) Electrical resistance of the optimized TEG (solid line/open marker) and load resistance (dashed line/filled marker) as a function of the ratio of external thermal resistances and (B) optimum load resistance to generator resistance ratio calculated using the multiparameter optimization simulation (solid line/open marker) and using the empirical temperature-dependent *ZT* relations with the average thermoelement temperature (dashed line/filled marker for three theoretical materials having peak $Z = 0.003\ K^{-1}$ at 400 K (gray), 600 K (blue), and 800 K (orange), respectively.

using Eq. (18) with transport properties at the average thermocouple temperature are plotted versus the external thermal resistance ratio with dashed lines/filled markers. We see that the results vary significantly, with the trend tending to be an overestimate of required load to TEG resistance ratio for maximum power transfer when using the common relation in Eq. (18), plotted as dashed lines with filled markers in Fig. 11B, which would result in non-optimized operation. This would translate to an electrical load design condition for the TEG which is smaller than it should be, meaning the TEG should be designed to be more electrically resistive than $m_{max\text{-}efficiency}$ would indicate for the majority of cases evaluated here.

5. Finite element simulations of common thermoelectric material structures

While the simulations presented in Section 4 are useful to isolate trends in the propagation of thermoelectricity physics, they are nevertheless based on idealized material systems. To see how these conclusions hold with materials measured in the literature, we examine the consequences of material temperature-dependence in more realistic scenarios through three n-/p-type pairs of representative high-performance materials with

maximum ZT at notably different temperatures: $Bi_2Te_{2.7}Se_{0.3}$ [21]/BiSbTe [22] with peak ZT near 100 °C, PbI_2-doped PbTe [23]/Na-doped PbTe [24] with peak ZT near 425 °C, and n-doped SiGe [25]/p-doped SiGe [26] with peak ZT near 900 °C. Due to their different temperature profiles, each of these pairs of materials would be best used in quite different applications. For example, the $Bi_2Te_{2.7}Se_{0.3}$/BiSbTe architecture may be used in a steam piping system, the PbI_2-doped PbTe architecture in a spacecraft power system, and the SiGe architecture in a high-temperature industrial waste heat recovery system or spacecraft power system. We use polynomial fits to capture the measured temperature-dependent transport properties for simulation in COMSOL™. Boundary conditions are selected for each pair to represent different regimes of operation and examine the behavior of TEG systems with peak ZT at different positions relative to the heat source and sink temperatures. Fig. 12 shows the calculated optimized load power and the corresponding fractional temperature drop across the thermoelements as a function of the ratio $R_{t,ext,c}/R_{t,ext,h}$.

Fig. 12 illustrates similar trends to the more idealized materials in Fig. 10. Again we see the inverse relationship between the load power and fractional temperature gradient, and the load power function generally following the shape of the figure of merit Z. The BiSbTe/BiTeSe and SiGe systems produce peak power when external thermal resistance is fully shifted to the heat source side ($R_{t,ext,c}/R_{t,ext,h} \ll 1$) resulting in lower average TEG temperatures, as their material parameters favor a higher Z value at the lower end of the temperature ranges considered. The PbTe system exhibits the opposite trend, favoring a shift of external thermal resistance to the cold sink side ($R_{t,ext,c}/R_{t,ext,h} \gg 1$), thus pushing the average TEG operating temperature toward the peak Z values at higher temperatures. Using a simple average of the n- and p-type Z values, we calculate the parameter β for each system within its respective reservoir temperatures to be $1.276 \times 10^{-3}\,K^{-1}$ (BiSbTe/BiTeSe between 300 and 473 K), $0.928 \times 10^{-3}\,K^{-1}$ (PbTe between 400 and 700 K), and $0.408 \times 10^{-3}\,K^{-1}$ (SiGe between 800 and 1200 K). Comparing β values directly is most relevant when choosing material candidates to operate within set reservoir temperatures, but we can infer from these calculations that the BiSbTe/BiTeSe scenario most effectively utilizes available system exergy.

In addition to the temperature dependence of the material Z values, we can further explain these trends by an analysis of the entropy generation in the system. Following the formulation presented by Ref. [27], exergy lost in the power generation system is derivable as:

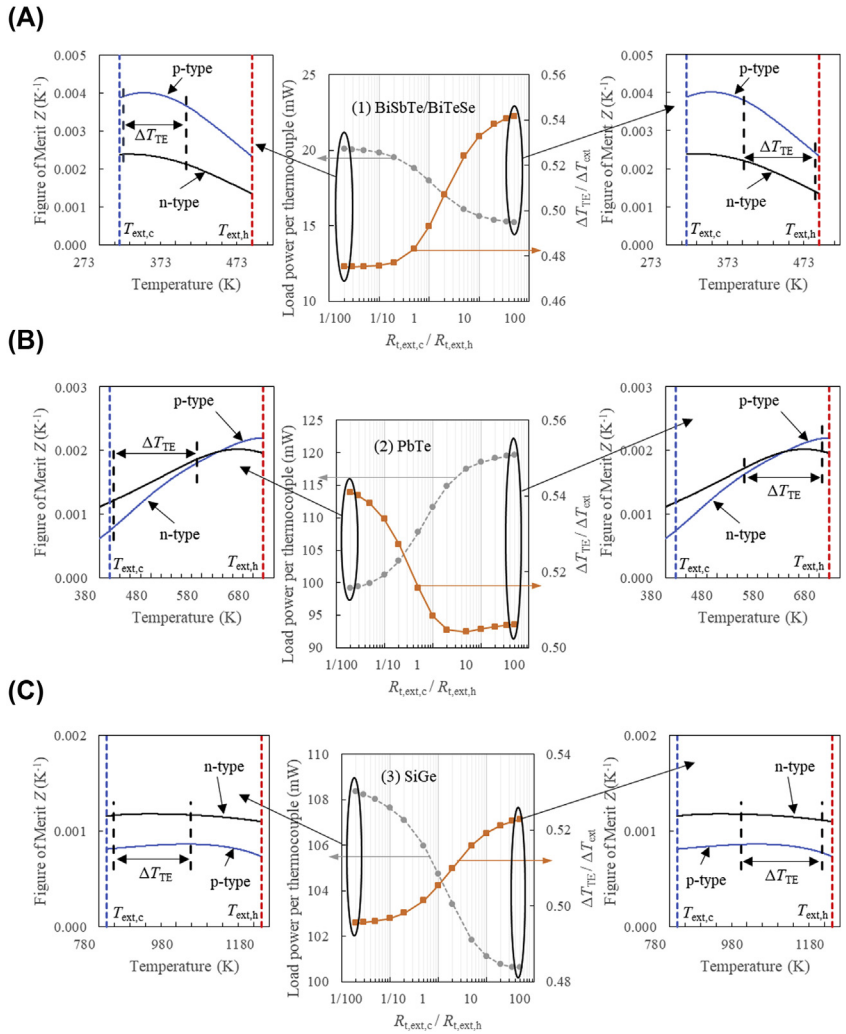

Fig. 12 Optimized load power per thermocouple and fractional temperature drop across thermoelements for (A) BiSbTe/BiTeSe, (B) PbTe, and (C) SiGe systems. For each case, the plot of n- and p-type material figure of merit is given, and the range of temperatures seen by the thermocouple producing the highest and lowest power output are shown.

$$\dot{X}_{lost} = \left(\dot{Q}_{h,rev} - \dot{Q}_{c,rev}\right) - \left(\dot{Q}_h - \dot{Q}_c\right) + \dot{Q}_h \frac{T_{ext,c}}{T_{TE,h}} - \dot{Q}_c \frac{T_{ext,c}}{T_{TE,c}} \tag{28}$$

In Eq. (28), the term the term $\left(\dot{Q}_{h,rev} - \dot{Q}_{c,rev}\right)$ represents the reversible work (*i.e.*, ideal power), while $\left(\dot{Q}_h - \dot{Q}_c\right)$ is the actual (non-ideal) work

produced by the TEG. We can express $\dot{Q}_c$ in terms of the TEG temperatures by relating it to the TEG efficiency as:

$$\dot{Q}_c = \dot{Q}_h - \dot{Q}_h \frac{\Delta T_{TE}}{T_{TE,h}} f(ZT) \tag{29}$$

The function $f(ZT)$ represents a modifier to the Carnot efficiency, first presented by Ref. [28] as:

$$f_{Ioffe} = \frac{\sqrt{1 + ZT_{avg}} - 1}{\sqrt{1 + ZT_{avg}} + \frac{T_{TE,c}}{T_{TE,h}}} \tag{30}$$

We continue with a generalized $f(ZT)$, which asymptotes at 1 in the limit of $ZT \rightarrow \infty$, noting the analysis by Ref. [29] demonstrating the limitations of ZT and the Ioffe $f(ZT)$ term when considering large temperature differences and temperature-dependent properties. Combining Eqs. (28) and (29) and rearranging yields the lost exergy as:

$$\dot{X}_{lost} = \left(\dot{Q}_{h,rev} - \dot{Q}_{c,rev}\right) - \left(\dot{Q}_h - \dot{Q}_c\right) - \dot{Q}_h \frac{T_{ext,c} \Delta T_{TE}}{T_{TE,h} T_{TE,c}} (1 - f(ZT)) \tag{31}$$

For constant reservoir temperatures, input heat load, and temperature drop across the TEG, the rate of entropy generation and effective lost exergy is minimized for the smallest $T_{TE,h}$ (the constant temperature drop assumption also simultaneously reducing $T_{TE,c}$). This is the same as all the external thermal resistance being on the hot side of the TEG. This lost exergy reduction is also associated with the decreasing $T_{TE,c}$ (*i.e.*, driving it toward $T_{ext,c}$) due to the reduction of cold-side thermal resistances relative to hot-side thermal resistances. Lost exergy is also decreased in a second scenario where the ΔT_{TE} is increased, with $T_{TE,h}$ increasing while simultaneously $T_{TE,c}$ decreases in this scenario. However, this condition competes with the coupling of the electrical and thermal systems in the TEG described in Section 2, where an increase in ΔT_{TE} for constant external thermal resistances requires an increase in the TEG thermal resistance, resulting in an increase in TEG electrical resistance. Under an operating condition of fixed external reservoir temperatures, ΔT_{TE} will increase asymptotically toward the limit of ΔT_{ext} with a linear increase in thermoelement length. However, the electrical resistance increases linearly with length (assuming temperature-independent properties), and losses from added electrical resistance will dominate gains from added ΔT_{TE} beyond $\Delta T_{TE}/\Delta T_{ext} \sim 0.5$. The final optimization

routine then becomes a function of the TEG material properties, geometry, and the thermal and electrical losses inside the TEG, which may compete with the effects of the external thermal irreversibilities through variations in the input heat load and the TEG efficiency. This is evident in the case of the PbTe system in this study, where Z strongly favors temperatures near the selected source temperature in contrast to the BiSbTe/BiTeSe system with Z strongly favoring temperatures near the sink temperature and the SiGe system which presents a more consistent Z versus T profile.

One of the most valuable insights here is in selecting the distribution of thermal interface materials in an assembly. Systems with large thermal gradients, especially across thin regions like in TEGs, experience significant thermal stresses. While a solid metallic bond is always preferred for its high thermal conductance, it is generally not possible to have both the hot and the cold side made of a rigid bond material due to thermal stresses induced by the large temperature gradients. Thus, at least one side must be a compliant material to ensure mechanical reliability, which almost always has lower thermal conductance due to the nature of thermal energy carrier conduction transport. This analysis demonstrates that in such a situation, the choice of placing the less thermally-conductive, compliant material on the hot or cold side of the system may have a significant impact on the resulting power output, and should generally be situated on the heat source-facing side, unless the material Z is sufficiently higher near the source temperature to offset lost exergy in the system. This is a convenient outcome in a way, as thermal conductivity of materials *generally* decreases with increasing temperature above room temperature. If a high conductance material were indicated for the high temperature side, it may require the use of more exotic, and more expensive, interface materials. Considering the Z temperature-dependency and exergy together is critical to determining the optimum distribution of external hot-side and cold-side thermal resistances and this can often times drive the system design to distributing the bulk of heat exchanger ΔT toward heat source facing side ($R_{t,ext,c}/R_{t,ext,h} < 1$). The temperature-dependence of the constituent thermoelectric material properties plays a strong role in establishing this optimum distribution. In general, in the absence of a thermoelectric figure of merit strongly favoring temperatures near the heat source temperature, this work shows that the second Law effects result in optimum system designs which drives a larger fraction of the external thermal resistance distribution to be located between the heat source and the TEG ($R_{t,ext,c}/R_{t,ext,h} << 1$).

6. Implications for system design with nano-engineered thermoelectric and heat transfer materials

We now consider the implications of the system design conclusions thus far on the design of materials at the nanoscale. The steady advancement in both the understanding of energy carrier physics at the nanoscale and the fabrication capabilities required to manipulate nanoscale transport characteristics has resulted in exciting implications for thermoelectric systems, spurring numerous research efforts in nanowires [30–32], nanotubes [33–36], and defect engineering [37–39], [57], [40,41]. The basis for motivation toward nanoengineered thermoelectrics is evident in Eq. (19), which suggests a desirable material exhibits a large Seebeck coefficient S, a high electrical conductivity σ, and a low thermal conductivity k. Qualitatively, this results in a material which will develop a large temperature gradient for a given heat input due to low k, which will then develop a large voltage due to large S, which will subsequently induce a large current due to large σ when connected to a load. A major challenge is that the parameters are fundamentally linked due to the nature of the energy carriers.

The Seebeck coefficient and electrical conductivity parameters are driven primarily by the distribution and transport of electrons within the material. In semiconductor materials near room temperature lattice waves can contribute to the phonon drag phenomenon which influences the thermoelectric field by "slowing down" electrons in the material. This results in a decreased electrical conductivity and an increased Seebeck coefficient, which follows the generally inverse relationship between the two parameters in a material. This complicates efforts to independently tune the Seebeck coefficient, which affects the electrical conductivity, and vice-versa.

In semiconductor materials, which are most frequently used in thermoelectric generator or heat pump applications due to their relatively high achievable figures of merit, both lattice waves (phonons) and electrons contribute significantly to the material's thermal conductivity at practical temperatures in an additive manner:

$$k = k_{phonon} + k_{electron} \tag{32}$$

The final component of the thermoelectric figure of merit Z is then coupled directly to the Seebeck coefficient and electrical conductivity via the electronic contribution to thermal conductivity, $k_{electron}$, which can be quantified with the Wiedemann-Franz-Lorenz law relating the electronic

thermal conductivity to the electrical conductivity σ for a nondegenerate semiconductor [58]:

$$\frac{k_{electron}}{\sigma} = 2\left(\frac{k_B}{e}\right)^2 T = \left(1.45 \times 10^{-8}\ V^2K^{-2}\right)\ T \tag{33}$$

In Eq. (33) we see that, when the Wiedemann-Franz-Lorenz relations hold, the ratio of electronic thermal conductivity to electrical conductivity remains approximately constant. This means that efforts to increase the electrical conductivity are likely to increase the thermal conductivity and reduce the ΔT developed across the thermocouple, and that efforts to reduce the electronic thermal conductivity are likely to increase the electrical resistance and reduce current and power. Engineering of the phonon contribution to thermal conductivity is then viewed as an opportunity to decouple the standard thermoelectric parameters, with the ideal material behaving as an "electron crystal-phonon glass" [42], retaining crystallographic order for electron transport but impeding lattice wave transport. One method for approaching this type of material behavior is the exploitation of the differences in mean free paths of phonons and electrons in certain materials. At the energy carrier level the thermal conductivity k can be simplified to an expression involving the carrier heat capacity C, velocity v, and mean free path λ, which represents the average distance traveled by that energy carrier prior to a scattering event:

$$k_i = \frac{1}{3} C_i v_i \lambda_i \tag{34}$$

In a perfect, infinite, single crystal material the only scattering mechanism is carrier-carrier interaction, either phonon-phonon or phonon-electron (electron-electron being a very minimal contribution). These interactions are governed by the material temperature which in turn determines the population and density of energy carriers and the frequency of scattering events. At typical operating temperatures, increasing material temperatures lead to increased scattering events for both phonon and electron carriers, resulting in decreased conductivity parameters through shortened mean free paths. In nondegenerate semiconductors, higher temperatures can push additional electrons into the conduction band which may compensate some of the losses in electronic thermal or electrical conductivity. However, above room temperature the trend is generally downward for both electrical and thermal conductivities with increasing temperature. We can connect the use of nanostructuring to decouple the electrical and thermal properties in some

materials to the findings in Sections 4 and 5 of this work by considering the relative impacts of geometric and energy carrier scattering contributions. Using Matthiessen's rule for a first-order evaluation of independent parallel scattering mechanisms, we consider a size effect of grain size (or single crystal film thickness) d in addition to phonon-phonon scattering:

$$\frac{1}{\lambda} = \frac{1}{\lambda_{p-p}} + \frac{1}{d} \tag{35}$$

Since the grain size is independent of temperature (in the absence of kinetic effects on the lattice), its introduction to the array of scattering mechanisms dampens the temperature-dependent impact of the bulk phonon-phonon scattering:

$$\frac{d}{dT}\left(\frac{1}{\frac{1}{\lambda_{p-p}(T)} + \frac{1}{d}}\right) = \frac{\lambda'_{p-p}(T)\, d^2}{\left(d + \lambda'_{p-p}(T)\right)^2} \tag{36}$$

Assuming that the scattering in a material will be more influenced by phonon-phonon interactions than phonon-grain boundary interactions at the higher temperatures available in an energy conversion system, and that the phonon-grain boundary interactions will more strongly contribute to the mean free path reduction at the lower end of the available temperature gradient, nanostructuring (in the absence of secondary effects) will cause the parameter Z to exhibit a flatter profile by way of the thermal conductivity with respect to temperature than in the material's bulk counterpart. We present a set of cases from the literature to both reinforce this concept and illustrate a counterpoint.

A comparison of SiGe ingot material used for RTG systems (solid lines) to nanostructured SiGe material (dashed lines) is provided in Fig. 13A. Calculating the ratio of ingot material to nanostructured material thermal conductivity and plotting on the right-side axis with open square markers, it is indeed clear that the nanostructuring results in a more pronounced thermal conductivity suppression at lower temperatures, and a "flattening" of the thermal conductivity profile. It was noted in the references that the electrical conductivity of the nanostructured materials remained largely unchanged from the ingot reference materials, and the authors concluded that the suppression in thermal conductivity was due to the lattice contribution.

A counter-example is shown in Fig. 13B for BiSbTe ingot and nanostructured material. The properties of BiSbTe result in electrons being

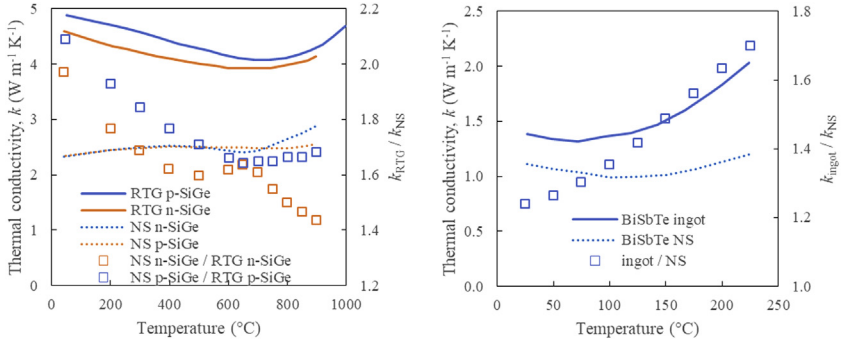

Fig. 13 Comparisons of bulk ingot and bulk nanostructured (NS) materials from literature, showing (A) p-type SiGe [26] and n-type SiGe [25], and (B) p-type BiSbTe [22]. Each plot shows reported bulk ingot (non-nanostructured) thermal conductivity, bulk NS thermal conductivity, and the ratio of ingot-to-NS.

excited into the conduction band at the higher temperatures, and while the lattice conductivity is indeed shown to be reduced through modeling of the Boltzmann Transport Equation, the increased electronic thermal conductivity begins to dominate the thermal transport relation given in Eq. (32). In this case the apparent reduction in thermal conductivity is more significant at the higher temperature range. However, the nanostructured thermal conductivity does demonstrate a notably flatter profile as suggested previously.

Generally, in the absence of secondary effects like enhanced conduction band excitation as in the case of BiSbTe, the temperature-independent contribution of grain boundary scattering is likely to further emphasize the optimization guideline for loading the bulk of external thermal resistance to the hot side of the system in order to drive down the average thermocouple temperature for any given hot source and cold ambient temperature combination and total external thermal resistance matching the TE internal thermal resistance.

There also has been progress in nano-engineered heat transfer materials and surfaces that can ultimately lead to more effective hot-side and cold-side heat exchangers with lower thermal resistances in advanced TEG systems. Recent research [43–48] has shown micro-engineered heat exchangers and nano-engineered surfaces that enhance heat transfer to dramatically reduce thermal resistances for TEG systems. Others [45,46] have demonstrated ultra-high heat fluxes (>1000 W cm^{-2}) on nano-engineered surfaces in microchannels that also provided more stable flow characteristics (*i.e.*, lower pressure fluctuations). Hendricks *et al.* [43] demonstrated high-heat flux (20 W cm^{-2}), low weight graphite heat exchanger designs having

low thermal resistance characteristics in thermoelectric systems. Sunada *et al.* [44] demonstrated high performance micro-engineered evaporator surfaces and wick structures that are 3-D printed with additive manufacturing techniques. Choi *et al.* [42] and Palko *et al.* [47,49] demonstrated nano-structured multi-mode (liquid and vapor) wicks in advanced micro- and nano-engineered evaporator surfaces that have demonstrated high-heat flux capabilities, reduced required superheats, and ability to operate more stably when compared with "bare" wicks and conventional microchannels. Miljkovic *et al.* [48] have developed advanced condensation heat transfer surfaces that experimentally demonstrated a 25% higher overall heat flux and 30% higher condensation heat transfer coefficient compared to state-of-the-art hydrophobic condensing surfaces at low supersaturations. This work demonstrates significant condensation heat transfer enhancement and promises a low cost and scalable approach to increase efficiency for applications such as atmospheric water harvesting, dehumidification, and high performance condensation heat exchangers. The results of these works contribute to the collective literature showing pathways and prototype demonstrations to significantly increased heat-flux designs, low-weight designs, and low thermal resistance designs that high-performance, cost-competitive TEG systems will require.

7. Thermoelectric system economics

Thermoelectric power technology can have key benefits and strengths in many terrestrial energy recovery applications. Earlier sections of this chapter have elucidated the importance of optimizing hot side and cold side thermal resistances and in particular the $(R_{t,ext,c}/R_{t,ext,h})$ ratios in a TEG system to maximize TEG power output. It is now equally important to consider the economic effects and costs associated with accomplishing this important design paradigm and implementing it in actual thermoelectric (TE) systems.

Thermoelectric system cost, G [\$ W^{-1}], and its dependency on TE converter fill factor, F, as defined below [18,50]:

$$F = A_{TE}/A_{HEX} \tag{37}$$

$$G = \frac{4\cdot(m+1)^2}{S_{net}{}^2\cdot\sigma\cdot m\cdot(T_{exh}-T_{amb})^2}\cdot\left[\frac{1.1\cdot\kappa_{TE}\cdot A_{HEX}\cdot F}{K_H}+l_{TE}\right]^2 \cdot\left[C''' + \frac{C''}{l_{TE}} + \frac{C_{HEX}\cdot UA_u}{A_{HEX}\cdot l_{TE}\cdot F}\right] \tag{38}$$

are key factors governing final decisions on using thermoelectric energy recovery systems in all terrestrial applications. Eq. (38) results when invoking the relationship $K_C \geq 10K_H$ from Ref. [15]. Thus, cost becomes as important as power density or efficiency in adoption of waste energy recovery (WER) thermoelectric generators (TEG). New integrated cost analysis/thermoelectric analysis approaches presented by Refs. [16,18,50,51] have shown key optimum [G_{opt}, F_{opt}] relationships and interdependencies between overall TEG system costs. These include TE material costs, manufacturing costs (specifically heat exchanger costs), and the TE performance design metrics such as TE material properties, TE device design parameters, heat exchanger performance metrics such as hot-side and cold-side conductances and UA values, and hot side heat flux in achieving optimal WER TEG designs. This new work is a more extensive, in-depth follow-up to fundamental work presented in [16,52,54]. A new paradigm in thermoelectric system economics has now emerged from these works that highlights and emphasizes how the thermoelectric system cost economics can be mathematically described and defined by a set of non-dimensional parameters shown in the equations below [18]:

$$F_{opt} = -\frac{1}{4}\cdot\left(\frac{\left(C_{HEX,h}+C_{HEX,c}\right)\cdot UA_u}{C'''\cdot {l_{TE}}^3 + C''\cdot {l_{TE}}^2}\right)\cdot\left(\frac{{l_{TE}}^2}{A_{HEX}}\right) + \frac{1}{4}\sqrt{\left(\frac{\left(C_{HEX,h}+C_{HEX,c}\right)\cdot UA_u}{C'''\cdot {l_{TE}}^3 + C''\cdot {l_{TE}}^2}\right)^2\cdot\left(\frac{{l_{TE}}^2}{A_{HEX}}\right)^2 + \frac{8}{1.1}\cdot\left(\frac{\left(C_{HEX,h}+C_{HEX,c}\right)\cdot UA_u}{C'''\cdot {l_{TE}}^3 + C''\cdot {l_{TE}}^2}\right)\cdot\left(\frac{{l_{TE}}^2}{A_{HEX}}\right)\left(\frac{K_H\cdot l_{TE}}{\kappa_{TE}\cdot A_{HEX}}\right)} \tag{39}$$

This optimum fill factor, F_{opt}, can then be substituted into G (Eq. 38) to obtain the optimum cost function, G_{opt}, which in turn can be mathematically manipulated to give a non-dimensional form of the optimum cost function given below:

$$\left[\frac{G_{opt}\left(\frac{\$}{W}\right)\cdot(S\cdot\Delta T)^2\cdot\sigma\cdot l_{TE}\cdot m}{4\cdot\left(C'''\cdot {l_{TE}}^3 + C''\cdot {l_{TE}}^2\right)\cdot(m+1)^2}\right] = \left(1+\frac{1.1\cdot\kappa_{TE}\cdot A_{HEX}\cdot F_{opt}}{K_H\cdot l_{TE}}\right)^2 \cdot\left[1+\left(\frac{\left(C_{HEX,h}+C_{HEX,c}\right)\cdot UA_u}{C'''\cdot {l_{TE}}^3 + C''\cdot {l_{TE}}^2}\right)\cdot\left(\frac{{l_{TE}}^2}{A_{HEX}\cdot F_{opt}}\right)\right] \tag{40}$$

where $\Delta T = (T_{exh} - T_{amb})$ links the cost impacts to the fundamental overall temperature differential in any given energy recovery application. Other parameters in Eqs. (39) and (40) are defined in the Nomenclature.

Eqs. (39) and (40) show that the optimum TEG cost conditions, F_{opt} and G_{opt}, are functions of three critical non-dimensional parameters:

$$\left(\frac{\left(C_{HEX,h}+C_{HEX,c}\right)\cdot UA_u}{C'''\cdot {l_{TE}}^3+C''\cdot {l_{TE}}^2}\right) \tag{41}$$

$$\left(\frac{{l_{TE}}^2}{A_{HEX}}\right) \tag{42}$$

$$\left(\frac{\kappa_{TE}\cdot A_{HEX}}{K_H\cdot l_{TE}}\right) \tag{43}$$

The first of these parameters is tied to the ratio of heat exchanger costs to TE device costs. The second parameter is coupled to TE device dimensions to TE/heat exchanger interfacial area (basically a geometric factor). The third parameter is tied directly to TE device/heat exchanger interfacial design parameters, heat exchanger UA_u and heat flux, ${q_h}''$. The third term is additionally tied directly to the hot-side interfacial heat flux, ${q_h}''$, by:

$$q_h''=\frac{K_H\left(T_{ext,h}-T_{TE,h}\right)}{A_{HEX}} \tag{44}$$

where K_H, the total hot side thermal conductance, is given by Refs. [18,50]:

$$K_H=\frac{\left(1-\chi_{TE,h}\right)}{\left[\frac{1}{\dot{m}_h C_p \varepsilon_h\left(1-\chi_{HEX,h}\right)}+\frac{1}{K_{HEX}}\right]} \tag{45}$$

as presented and discussed by Refs. [18,50]. The first term in the denominator is the caloric heat transfer performance of the heat exchanger determined by its mass flow rate, fluid specific heat, and heat exchanger effectiveness, ε_h. The second term in the denominator associated with K_{HX} is the sum effect of all thermal interface conductances (resistances) between the heat exchanger and the TE device hot side. $\chi_{TE,h}$ and $\chi_{HEX,h}$ are fractional thermal loss terms at the TE/heat exchanger hot side interface and within the heat exchanger itself as defined and discussed in Refs. [18,50]. It is clear upon examining Eqs. (44) and (45) that the hot-side interfacial heat flux, ${q''}_h$, is then a function of not only the heat exchanger caloric performance, but also the interfacial thermal conductances (resistances) between the TE device and the hot side heat exchanger.

A fundamental TE materials cost parameter (in \$ W^{-1}) is evident in Eq. (46) defined by:

$$G_o^*\left[\frac{\$}{W}\right] = \frac{4\cdot\left(C'''\cdot l_{TE}{}^3 + C''\cdot l_{TE}{}^2\right)\cdot(m+1)^2}{(S_{net}\cdot\Delta T)^2\cdot\sigma\cdot l_{TE}\cdot m} = \frac{4\cdot C''\cdot l_{TE}\cdot\left(\frac{C'''\cdot l_{TE}}{C''}+1\right)\cdot(m+1)^2}{(S_{net}\cdot\Delta T)^2\cdot\sigma\cdot m} \tag{46}$$

such that G_{opt}/G_o^* is defined by Eq. (40) above, where $\Delta T = (T_{exh} - T_{amb})$ links the cost impacts to the fundamental temperature differential in any given energy recovery application. Eqs. (40) and (46) clearly reveal that energy recovery applications with larger available temperature differentials will have cost advantages and research, development, and deployments should preferentially target these. The second form for G_o^* reveals a fourth non-dimensional parameter:

$$\left(\frac{C'''\cdot l_{TE}}{C''}+1\right)$$

that can also be extracted from the first two non-dimensional parameters above (Eqs. 41 and 42). This parameter essentially describes the ratio between TE material volumetric costs and TE manufacturing costs and their relative impact on overall TEG system costs. This parameter also is fundamental to determining the relative importance of TE volumetric costs and manufacturing costs and is discussed at length by Ref. [18] in mapping out various influential cost regimes.

Eqs. (39) and (40) define the inherent relationships and interdependencies between TE material costs, manufacturing costs and heat exchanger costs, and the TE performance design metrics such as TE material properties, TE device design parameters, heat exchanger performance metrics such as hot-side and cold-side conductances and UA values, and hot side heat flux in achieving optimal cost WER TEG designs. These relationships include critical constraints defined and controlled by the critical parameters given in Eqs. (41)—(43) that lead to the most cost-effective WER TEG designs approaching \$1-\$3 W^{-1}, as discussed by Ref. [18]. One key finding that represents a new design paradigm in thermoelectric system design is that Eqs. (39) and (40), which predict optimum TEG cost conditions, generally tend to predict high fill factors, F_{opt}, (*i.e.*, values of 0.6—1.0) under most conditions to obtain cost-effective TEG designs. This is because high heat exchanger costs put a premium value on the heat exchanger area, A_{HEX}, and requires the TE devices to fully utilize the heat exchanger area in an optimum cost design. This is much higher than conventional TE systems use

and represents a dramatic shift in thinking; common industry practice driven by manufacturing constraints is $F \cong 0.2$. However, higher fill factors as predicted with this work are consistent with cost-effective solar photovoltaic power technologies and solar array designs that generally also want high active-area-to-total-area ratios (the comparable metric to F). This industry has mastered the manufacturing challenges to achieve such a design condition and cost effective systems. The solar photovoltaic industry generally achieves active-area-to-total-area ratios in solar cell design of >0.95 in its cost-effective designs, so it is actually not that surprising cost-effective TEG systems should require high F values. The thermoelectric industry should expect to address and conquer the same type of manufacturing challenges to achieve cost-effective, cost-competitive TEG designs.

It is critical to point out when using Eqs. (39) and (40) that a key inherent relationship embedded within Eq. (39) is that there is a limiting hot-side heat flux that is tied to TE material properties, TE device design parameters, and TE material costs, associated with maintaining $F_{opt} \leq 1$. This limited heat flux relationship is given by:

$$q''_{h,HEX} \leq \frac{2.2 \cdot \kappa_{TE} \cdot (T_{exh} - T_{hot})}{l_{TE}} \cdot \left[\frac{1}{\left(\frac{(C_{HEX,h} + C_{HEX,c}) \cdot UA_u}{C''' \cdot l_{TE}^3 + C'' \cdot l_{TE}^2} \right) \cdot \left(\frac{l_{TE}^2}{A_{HEX}} \right)} + \frac{1}{2} \right] \tag{47}$$

This Eq. (47) must be used when using Eq. (39) because it is a geometric relationship, whereas Eq. (47) invokes and applies interfacial energy conservation throughout its region of application with Eq. (39). This equation is revolutionary in itself because it basically states that in cost-effective, cost-competitive TE systems, the required TE device hot side heat flux is coupled to not only TE materials and TE device design parameters, but also heat exchanger and TE material costs.

New work has further examined key heat flux and heat exchanger cost sensitivities and interrelationships using the new optimum [G_{opt}, F_{opt}] relationships to show the dominating role TEG hot-side heat flux plays in new thermoelectric system economics (TSE) paradigms. Fig. 14 demonstrates and quantities the relationship between TEG system cost and TEG hot-side heat flux. This figure plots the TEG system cost, G_{opt}, shown in Eq. (40) as a function of hot-side heat flux given in Eq. (44) for different assumptions and metrics on L_{TE} (TE element length dimension), heat

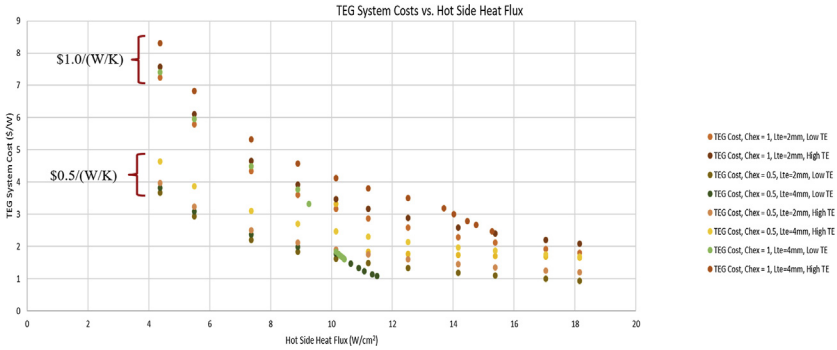

Fig. 14 TEG System Cost Dependence on TEG Hot Side Heat Flux, TE material and manufacturing costs, and TE element dimensions. Computations use $L_{TE} = 0.002-0.004$ m, $k_{TE} = 2.41$ W m^{-1}K^{-1}, $A_{HEX} = \sim 0.007$ m^2.

exchanger cost parameter, C_{HEX}, and the TE materials and manufacturing costs. The difference between high and low TE costs is a factor of 5X on both C''' and C'' in this investigation, *e.g.* $C'''_{high} = 5\ C'''_{low}$ and similarly for C''. What is apparent in Fig. 14 is that the TEG system cost reduces dramatically (by factors of ~4X) as hot side heat flux applied at the TE converter increases from 4 W cm^{-2} up to 18–20 W cm^{-2} and the heat exchanger cost parameter, C_{HEX}, is reduced by a factor of 2X from \$1 (W K^{-1})$^{-1}$ to \$0.5 (W K^{-1})$^{-1}$. It is apparent that as hot side heat flux increases toward 18–20 W cm^{-2} that TEG costs also achieve a cost asymptote nearing \$1-\$2 W^{-1}, such that higher hot side heat fluxes are inconsequential; however even reaching this 18–20 W cm^{-2} level in advanced TEG systems will require new and unique high performance heat exchangers that must also be low cost.

Fig. 14 data is interesting in another aspect related to Eq. (47) above. In three of the cases shown in Fig. 14 associated with longer TE element lengths, $l_{TE} = 4$ mm.

- $C_{Hex} = 1$, $l_{TE} = 4$ mm, Low TE Costs
- $C_{Hex} = 1$, $l_{TE} = 4$ mm, High TE Costs
- $C_{Hex} = 0.5$, $l_{TE} = 4$ mm, Low TE Costs

One can see an apparent "kink" or change in slope in the cost versus heat flux curve and then the cost curve stopping at lower heat flux values than the other curves. This is a direct result of applying the limiting heat flux condition described in Eq. (47) to [G_{opt}, F_{opt}] computations and the effect of considering longer TE element lengths, l_{TE}. While TEG costs, G_{opt}, does continue to drop as hot side heat flux increases, at this point heat flux

increases are slower and more difficult (and possibly impossible) to achieve because they must be simultaneously accompanied by heat exchanger area, A_{HEX}, increases to satisfy the $F_{opt} \leq 1$ and Eq. (47) conditions.

This work elucidates a new TSE paradigm that indicates hot-side heat flux plays a more influential role than TE material costs themselves or TE device geometry factors in reducing TEG system costs toward the elusive \$1-\$3 W^{-1} range. Current results show a four-fold increase in hot-side heat flux can decrease TEG system costs by approximately four times and has a more dramatic effect on TEG system costs than a five-fold decrease in TE material and manufacturing costs or a four-fold decrease in TE couple dimensions. Raw heat exchanger costs [\$ $(W K^{-1})^{-1}$] to achieve the high heat flux conditions also have a dominating influence.

This work on thermoelectric system economics and the inherent paradigm shifts it infers has serious implications on TEG system design in terrestrial WER applications. This cost analysis work now also shows the importance that optimizing hot-side and cold-side heat exchanger performance, in particular increasing hot-side heat flux, has on decreasing TEG system costs. The requirement that high hot side heat flux in TEG systems creates more cost-competitive TEG system costs is clear and is consistent with similar requirements for high incoming solar irradiance (i.e., fluxes) in solar thermal and solar photovoltaic systems to create cost-competitive solar systems. This work provides a framework and methodology for determining how to distribute and focus heat exchanger costs (both developmental and recurring costs) to produce high-performance, cost-effective TEG system design.

8. Conclusions

In this chapter, we have presented evaluations of various aspects of system design in thermoelectric generators (TEGs). TEGs represent highly-coupled and complex thermal systems which are sensitive to parameters at the nanoscale through the manipulation of thermal and electrical energy carriers, all the way up to the balancing of external thermal resistances in the heat exchangers coupling the TEG to the heat source and sink thermal reservoirs. By a careful and systematic evaluation of the impacts of thermoelectric phenomena, temperature-dependent material properties, and the relative loading of external thermal resistances in the thermal system design, we are able to isolate specific trends to advise the system-level design of

TEG power converters. We show primary competing mechanisms in the selection of TEG operating temperature to be the temperature dependence of the thermoelectric material Z values and the thermodynamic effects of exergy loss. When the Z versus T profile is relatively flat or strongly favors lower temperatures, the highest load power output is achieved when the TEG operating temperature is shifted toward the heat sink temperature and $R_{t,ext,c}/R_{t,ext,h} < 1$. Possibly in contradiction of intuition, it is only favorable to shift the average TEG temperature toward the high end of the temperature range when Z strongly favors higher temperatures. This behavior is not seen when the analysis does not consider Peltier effects, indicating the importance of including the Peltier effect from a second Law perspective.

Nano-engineering of materials fundamentally contributes to a "flattening" of temperature-dependent thermal conductivity, primarily in the lattice conductivity component. If secondary effects such as electron excitation are not significant, this effect may serve in some materials to dampen any strong relative reductions in thermal conductivity at higher temperatures where phonon-phonon scattering is expected to dominate phonon-boundary scattering. In the context of the findings of the loss exergy analysis, this suggests that nanostructured materials which promote phonon-boundary scattering may do so disproportionately at lower temperatures, further favoring a distribution of external resistances weighted toward the hot side which drives the TEG operating point to lower temperature. Micro-engineered heat exchangers and nano-engineered heat transfer surfaces have shown the pathways, approaches and techniques required in high-performance, low-thermal- resistance heat exchangers to satisfy requirements necessary to achieve high-performance, cost-effective TEG systems.

Finally, a new thermoelectric system cost/performance analysis paradigm is presented that accounts for TE material costs, TE manufacturing costs, and heat exchanger costs in a unified model using non-dimensional analyses. Critical non-dimensional parameters are identified that control overall TEG system costs and elucidate the critical interdependencies between key TE material and manufacturing costs, heat exchanger costs, and TE and heat exchanger design and performance parameters in determining overall TEG system costs. This new TE system economic model clearly shows what parameter interrelationships govern and control costs and what TE/heat exchanger cost and performance parameters drive and dominate the overall TEG costs. The new TE system economic/

performance analysis demonstrates the critical economic considerations of external heat exchanger design in overall TEG system optimization. New analyses demonstrate that increased heat fluxes at the hot side heat exchanger can dominate in decreasing TEG system cost in terms of a \$ W^{-1} metric. It has been shown that the hot-side heat flux and heat exchanger costs are more influential than TE material and manufacturing costs in achieving cost-competitive TEG designs. The collective framework in this chapter provides systematic guidelines for improving the performance and cost-competitiveness of TEG systems in a comprehensive, multi-scale analysis enlightening to thermoelectric systems engineers and informative for readers interested in the design and optimization of complex thermal systems.

Authors

Marc T. Dunham completed his B.S. Physics (2010), B.M.E. Mechanical Engineering (2010), and M.S. Mechanical Engineering (2012) at the University of Minnesota – Twin Cities, before completing his Ph.D. in Mechanical Engineering (2016) at Stanford University as an NDSEG Fellow under the advisement of Professor and Department Chair Kenneth E. Goodson. His work experience includes time at the NASA Jet Propulsion Laboratory, Sandia National Laboratories, and Analog Devices, Inc., and general areas of research interest include thermal science, thermoelectric phenomena and devices, concentrated solar power, and nanoscale thermal transport.

Terry J. Hendricks is currently a Project Manager, an ASME Fellow, and IEEE Senior Member in the Power and Sensor Systems Section, Autonomous Systems Division at NASA—Jet Propulsion Laboratory (JPL)/California Institute of Technology, Pasadena, CA. He has recently been inducted into the University of Texas at Austin Mechanical Engineering Academy of Distinguished Alumni. He has over 39 years of professional experience and expertise in thermal & fluid systems, energy recovery, energy conversion and energy storage systems, terrestrial and spacecraft power systems, micro electro-mechanical systems, and project management, resulting in numerous journal and conference publications and US DOE National Laboratory and NASA performance awards and recognitions. Dr. Hendricks received his Ph.D. and Master of Science in Engineering from the University of Texas at Austin and Bachelor of Science (Summa Cum Laude) in Physics from the University of Massachusetts at Lowell.

Kenneth E. Goodson chairs the Mechanical Engineering Department at Stanford University, where he holds the Davies Family Provostial Professorship. He is a heat transfer specialist with 40 PhD alumni, nearly half of whom are professors at schools including Stanford, Berkeley, and MIT. Goodson is a Fellow with ASME, IEEE, AAAS, and APS. Honors include the ASME Kraus Medal, the ASME Heat Transfer Memorial Award, the AIChE Kern Heat Transfer Award, the THERMI award, and the SRC Technical Excellence Award. Goodson co-founded Cooligy, which developed cooling systems for Apple desktops. Goodson's MIT education includes the B.S. (1989) and Ph.D. (1993) in Mechanical Engineering.

Acknowledgments

This work was carried out as part of the NASA Prime contract NNN12AA01C at the Jet Propulsion Laboratory, California Institute of Technology, under a contract to the National Aeronautics and Space Administration. The cost information contained in this document is of a budgetary and planning nature and is intended for informational purposes only. It does not constitute a commitment on the part of Jet Propulsion Laboratory and/or California Institute of Technology.

References

[1] J.R. Salvador, J.Y. Cho, Z.X. Ye, J.E. Moczygemba, A.J. Thompson, J.W. Sharp, et al., Thermal to electrical energy conversion of skutterudite-based thermoelectric modules, J Electron Mater 42 (2013) 1389–1399.
[2] Yanliang Zhang, Martin Cleary, Xiaowei Wang, Nicholas Kempf, Luke Schoensee, Jian Yang, Giri Joshi, Lakshmikanth Meda, High-temperature and high-power-density nanostructured thermoelectric generator for automotive waste heat recovery, Energy Conversion and Management 105 (2015) 946–950.
[3] D.T. Crane, Journal of Electronic Materials 40 (2011) 561.
[4] D.T. Crane, J.W. LaGrandeur, L.E. Bell, Progress Report on BSST Led, U.S. DOE Automotive Waste Heat Recovery Program, Journal of Electronic Materials 39 (9) (2010) 2142–2148.
[5] T.J. Hendricks, W. Choate, U.S. Department of Energy, Office of Energy Efficiency & Renewable Energy Industrial Technology Program (ITP), 2006 Report Entitled: "Engineering Scoping Study of Thermoelectric Generator Systems for Industrial Waste Heat Recovery", 2006. PNNL-16196, http://www.eere.energy.gov/industry/imf/analysis.html.
[6] L.E. Bell, Cooling, heating, generating power, and recovering waste heat with thermoelectric systems, Science 321 (5895) (2008) 1457–1461.
[7] A. Shakouri, Recent developments in semiconductor thermoelectric physics and materials, Annu. Rev. Mater. Res. 41 (1) (2011) 399–431.
[8] A. Shakouri, Nanoscale thermal transport and microrefrigerators on a chip, Proc. IEEE (2006) 1613–1638.
[9] A.Z. Sahin, B.S. Yilbas, The thermoelement as thermoelectric power generator: effect of leg geometry on the efficiency and power generation, Energy Convers. Manag. 65 (2013) 26–32.

[10] J.H. Meng, X.X. Zhang, X.D. Wang, Multi-objective and multi-parameter optimization of a thermoelectric generator module, Energy 71 (2014) 367–376.
[11] M.T. Dunham, M.T. Barako, S. LeBlanc, M. Asheghi, B. Chen, K.E. Goodson, Power density optimization for micro thermoelectric generators, Energy 93 (2) (2015) 2006–2017.
[12] T.J. Hendricks, J.A. Lustbader, Advanced thermoelectric power system investigations for light-duty and heavy duty applications. II, in: Proceedings of the 21st International Conference on Thermoelectrics, 2002, pp. 387–394.
[13] Y. Apertet, H. Ouerdane, O. Glavatskaya, C. Goupil, P. Lecoeur, Optimal working conditions for thermoelectric generators with realistic thermal coupling, Europhysics Letters Association 97 (2) (2012).
[14] K. Yazawa, A. Shakouri, Cost-efficiency trade-off and the design of thermoelectric power generators, Environ. Sci. Technol. 45 (17) (2011) 7548–7553.
[15] T.J. Hendricks, "Integrated thermoelectric–thermal system resistance optimization to maximize power output in thermoelectric energy recovery systems" 1642, Materials Research Society, 2014 https://doi.org/10.1557/opl.2014.443 mrsf13-1642-bb02-04. Mater. Res. Soc. Symp. Proc.
[16] T.J. Hendricks, S.K. Yee, S. LeBlanc, Cost-scaling of a real-world exhaust waste heat recovery thermoelectric generator: a deeper dive, J. Electron. Mater. 45 (3) (2015) 1751–1761.
[17] K. Yazawa, A. Shakouri, T.J. Hendricks, Thermoelectric heat recovery from glass melt processes, Energy 118 (2017) 1035–1043.
[18] T.J. Hendricks, Thermoelectric system economics: where the laws of thermoelectrics, thermodynamics, heat transfer and economics intersect, MRS Advances 4 (8) (2019) 457–471.
[19] K. Yazawa, A. Shakouri, Energy payback optimization of thermoelectric power generator systems, in: Proceedings of the ASME 2010 International Mechanical Engineering Congress & Exposition, Nov. 12–18, 2010, Vancouver, British Columbia, Canada, 2010.
[20] J.W. Stevens, Optimal design of small ΔT thermoelectric generation systems, Energy Convers. Manag. 42 (2001) 709–720.
[21] X. Yan, B. Poudel, Y. Ma, W.S. Liu, G. Joshi, H. Wang, Y. Lan, D. Wang, G. Chen, Z.F. Ren, Experimental studies on anisotropic thermoelectric properties and structures of n-type $Bi_2Te_{2.7}Se_{0.3}$, Nano Lett. 10 (9) (2010) 3373–3378.
[22] B. Poudel, Q. Hao, Y. Ma, Y. Lan, A. Minnich, B. Yu, X. Yan, D. Wang, A. Muto, D. Vashaee, X. Chen, J. Liu, M.S. Dresselhaus, G. Chen, Z. Ren, High-thermoelectric performance of nanostructured Bismuth Antimony Telluride bulk alloys, Science 320 (5876) (2008) 634–638.
[23] A.D. LaLonde, Y. Pei, G.J. Snyder, Reevaluation of $PbTe_{1-x}I_x$ as high performance n-type thermoelectric material, Energy Environ. Sci. 4 (6) (2011) 2090–2096.
[24] Y. Pei, A. LaLonde, S. Iwanaga, G.J. Snyder, High thermoelectric figure of merit in heavy hole dominated PbTe, Energy Environ. Sci. 4 (6) (2011) 2085–2089.
[25] X.W. Wang, H. Lee, Y.C. Lan, G.H. Zhu, G. Joshi, D.Z. Wang, J. Yang, A.J. Muto, M.Y. Tang, J. Klatsky, S. Song, M.S. Dresselhaus, G. Chen, Z.F. Ren, Enhanced thermoelectric figure of merit in nanostructured *n*-type silicon germanium bulk alloy, Appl. Phys. Lett. 93 (19) (2008) 193121.
[26] G. Joshi, H. Lee, Y. Lan, X. Wang, G. Zhu, D. Wang, R.W. Gould, D.C. Cuff, M.Y. Tang, M.S. Dresselhaus, G. Chen, Z. Ren, Enhanced thermoelectric figure-of-merit in nanostructured p-type silicon germanium bulk alloys, Nano Lett. 8 (12) (2008) 4670–4674.
[27] J.R. Howell, R.O. Buckius, Fundamentals of Engineering Thermodynamics – English/SI Version, McGraw-Hill, Inc., 1987.

[28] A.F. Ioffe, Thermoelements, Semiconductor, and Thermoelectric Cooling, Infosearch Ltd., London, England, 1957.
[29] H.S. Kim, W. Liu, G. Chen, C.W. Chu, Z. Ren, Relationship between thermoelectric figure of merit and energy conversion efficiency, Proc. Natl. Acad. Sci. 112 (27) (2015) 8205–8210.
[30] Y.M. Lin, X. Sun, M.S. Dresselhaus, Theoretical investigation of thermoelectric transport properties of cylindrical Bi nanowires, Phys. Rev. B 62 (7) (2000) 4610.
[31] A.I. Hochbaum, R. Chen, R.D. Delgado, W. Liang, E.C. Garnett, M. Najarian, A. Majumdar, P. Yang, Enhanced thermoelectric performance of rough silicon nanowires, Nature 451 (7175) (2008) 163.
[32] A. Boukai, Y. Bunimovich, J. Tahir-Kheli, J.K. Yu, W.A. Goddard, J.R. Heath, Silicon nanowires as efficient thermoelectric materials, in: Materials for Sustainable Energy, 2011, pp. 116–119.
[33] J. Hone, I. Ellwood, M. Muno, A. Mizel, M.L. Cohen, A. Zettl, A.G. Rinzler, R.E. Smalley, Thermoelectric power of single-walled carbon nanotubes, Phys. Rev. Lett. 80 (5) (1998) 1042.
[34] X.B. Zhao, X.H. Ji, Y.H. Zhang, T.J. Zhu, J.P. Tu, X.B. Zhang, Bismuth telluride nanotubes and the effects on the thermoelectric properties of nano-tube containing nanocomposites, Appl. Phys. Lett. 86 (2005) 062111.
[35] Q. Yao, L. Chen, W. Zhang, S. Liufu, X. Chen, Enhanced thermoelectric performance of single-walled carbon nanotubes/polyaniline hybrid nanocomposites, ACS Nano 4 (4) (2010) 2445–2451.
[36] C. Meng, C. Liu, S. Fan, A promising approach to enhanced thermoelectric properties using carbon nanotube networks, Adv. Mater. 22 (4) (2010) 535–539.
[37] J.K. Yu, S. Mitrovic, D. Tham, J. Varghese, J.R. Heath, Reduction of thermal conductivity in phononic nanomesh structures, Nat. Nanotechnol. 5 (2010) 718–721.
[38] Y. Pei, H. Wang, G.J. Snyder, Band engineering of thermoelectric materials, Adv. Mater. 24 (46) (2012) 6125–6135.
[39] L. Hu, T. Zhu, X. Liu, X. Zhao, Point defect engineering of high-performance bismuth-telluride-based thermoelectric materials, Adv. Funct. Mater. 24 (33) (2014) 5211–5218.
[40] M.T. Dunham, B. Lorenzi, S.C. Andrews, A. Sood, M. Asheghi, D. Narducci, K.E. Goodson, Enhanced phonon scattering by nanovoids in high thermoelectric power factor polysilicon thin films, Appl. Phys. Lett. 109 (2016) 253104.
[41] B. Lorenzi, R. Dettori, M.T. Dunham, C. Melis, R. Tonini, L. Colombo, A. Sood, K.E. Goodson, D. Narducci, Phonon scattering in silicon by multiple morphological defects: a multiscale analysis, J. Electron. Mater. 47 (9) (2018) 5148–5157.
[42] G.A. Slack, in: D.M. Rowe (Ed.), "New Materials and Performance Limits for Thermoelectric Cooling" in CRC Handbook of Thermoelectrics, CRC Press, Boca Raton, FL, 1995.
[43] T.J. Hendricks, B. Mcenerney, F. Drymiotis, B.I. Furst, A. Shevade, Design and testing of high-performance mini-channel graphite heat exchangers in thermoelectric energy recovery systems, in: ASME 2017 15th International Conference on Nanochannels, Microchannels, and Minichannels, Technical Presentation #ICNMM201705583, Cambridge, MA, 2017 and Proceedings of ASME International Mechanical Engineering Congress and Exposition 2017, Paper #IMECE2017-72411, American Society of Mechanical Engineers Publishing, Tampa, FL, 2017.
[44] E. Sunada, B. Furst, P. Bhandari, B. Carroll, G.C. Birur, T. Hendricks, J. Kempenaar, H. Nagai, T. Daimaru, K. Sakamoto, S. Cappucci, J. Mizerak, A two-phase mechanically pumped fluid loop for thermal control of deep Space science missions, in: Proceedings of 46th International Conference on Environmental Systems ICES-2016-129, Paper #ICES-2016-129, Vienna, Austria, 2016.

[45] Y. Zhu, D.S. Antao, K.-H. Chu, S. Chen, T.J. Hendricks, T. Zhang, E.N. Wang, Surface structure enhanced microchannel flow boiling, J. Heat Transf. 138 (9) (2016) 091501, https://doi.org/10.1115/1.4033497. Transaction of the American Society of Mechanical Engineers, New York.
[46] Y. Zhu, D.S. Antao, K.-H. Chu, T.J. Hendricks, E.N. Wang, Enhanced flow boiling heat transfer in microchannel with structured surfaces, in: Proceedings of the 15th International Heat Transfer Conference, IHTC-15, Paper #IHTC15-9508, Kyoto, Japan, 2014.
[47] C. Choi, C.-H. Chang, S. Krishnan, T.J. Hendricks, W. TeGrotenhuis, Capillary rise and evaporative heat transfer in nano-structured multi-mode wicks, in: Proceedings of the ASME International Mechanical Engineering Congress & Exposition, IMECE 2011, ASME, New York, November 2011. Paper # IMECE2011-63776.
[48] N. Miljkovic, R. Enright, Y. Nam, K. Lopez, N. Dou, J. Sack, E.N. Wang, Jumping-droplet-enhanced condensation on scalable superhydrophobic nanostructured surfaces, Nano Lett. 13 (1) (2013) 179−187, https://doi.org/10.1021/nl303835d (American Chemical Society).
[49] J.W. Palko, H. Lee, C. Zhang, T.J. Dusseault, T. Maitra, Y. Won, D.D. Agonafer, J. Moss, F. Houshmand, G. Rong, J.D. Wilbur, D. Rockosi, I. Mykyta, D. Resler, D. Altman, M. Asheghi, J.G. Santiago, K.E. Goodson, Extreme two-phase cooling from laser-etched diamond and conformal, template-fabricated microporous copper, Adv. Funct. Mater. 27 (45) (2017).
[50] T.J. Hendricks, Heat exchanger performance impacts on optimum cost conditions in thermoelectric energy recovery designs, Mater. Today: Proceedings 5 (4) (2018) 10357−10370.
[51] T.J. Hendricks, New paradigms in defining optimum cost conditions in thermoelectric energy recovery designs, Mater. Today: Proceedings 8 (2) (2019) 613−624.
[52] S.K. Yee, S. LeBlanc, K.E. Goodson, C. Dames, $ per W metrics for thermoelectric power generation: beyond ZT, Energy Environ. Sci. 6 (9) (2013) 2561−2571.
[53] S.W. Angrist, Direct Energy Conversion, fourth ed., Allyn and Bacon, Boston, MA, 1982.
[54] S. LeBlanc, S.K. Yee, M.L. Scullin, C. Dames, K.E. Goodson, Material and manufacturing cost considerations for thermoelectrics, Renew. Sustain. Energy Rev. 32 (2014) 313−327.
[55] Y.S. Touloukian, Thermophysical Properties of High Temperature Solid Materials, Volume 4, Part 1, Thermophysical and Electronic Properties Information Analysis Center, Lafayette, IN, USA, 1966.
[56] L. Yang, Z.G. Chen, M.S. Dargusch, J. Zou, High performance thermoelectric materials: progress and their applications, Advanced Energy Materials 8 (6) (2018).
[57] B. Lorenzi, D. Narducci, R. Tonini, S. Frabboni, G.C. Gazzadi, G. Ottaviani, N. Neophytou, X. Zianni, Paradoxical enhancement of the power factor of polycrystalline silicon as a result of the formation of nanovoids, J. Electron. Mater. 43 (10) (2014) 3812−3816.
[58] C. Chiritescu, C. Mortensen, D.G. Cahill, D. Johnson, P. Zschack, Lower limit to the lattice thermal conductivity of nanostructured Bi2Te3-based materials, J. Appl. Phys. 106 (2009) 073503.